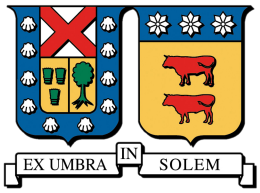

Universidad Técnica Federico Santa María

Department of Physics

Interaction of Liquids with Nanostructured Surfaces

by
Diego Ignacio Cortés Garcés

A thesis Submitted for the Degree of
Master of Science in Physics

Supervisor : Dr. Tomás P. Corrales
Thesis Committee : Dr. Valeria del Campo
Dr. Michael Kappl

June 2022

To my parents, my sister, my friends
and all the people who encouraged me to follow this path.

Acknowledgments

I would like to acknowledge ANID for supporting my research stay in Germany by funding grant project PCI Conicyt-Max Planck MPG190023 and the funding grant Fondecyt Regular 1211901. Special thanks for my advisors at MPIP, Michael Kappl and Hans-Jürgen Butt, and my advisor in Chile, Tomas P. Corrales at UTFSM, who gave me the chance to take on this project. Finally yet importantly, I have to give my thanks to Sajjad Shumaly for providing support in the image processing and all the MPIP AK Butt Group.

Abstract

The study and characterization of wetting properties is a crucial first step in achieving a fundamental understanding and specific development of superhydrophobic and superamphiphobic surfaces. In this context, static and dynamic contact angle measurements are the main techniques widely used to characterize wetting behavior of surfaces. However, these macroscopic techniques leave a lack of knowledge of what is happening at the surface itself at the submicroscopic level. Here, repellent surfaces (superhydrophobic and superamphiphobic) have been prepared and their adhesion force with micron-sized droplets have been measured using Atomic Force Microscopy (AFM).
In this way, AFM has allowed us to measure forces of nN of resolution, thereby making it possible to determine the adherence of micro-sized drops with the surface. We achieved this by attaching a liquid drop to the end of a tip-less cantilever (droplet probe) and performed force spectroscopy. For this we have used ionic liquids and water-glycerol mixtures to obtain droplets with microscopic radius and little loss of mass due to evaporation. Moreover, Confocal microscopy has been combined with AFM to visualize the droplet behaviour during the force measurement, this powerful tool allows us to observe the drop deformation, the contact angle and the pinning area of the drop. Also, we can determine if there is some remnant of the droplet left on the surface, due to the quality of the repellent surface.

Contents

1 Introduction **7**
- 1.1 Motivations and Thesis Outline . . . 7
- 1.2 Droplet Interface Interactions . . . 9
  - 1.2.1 Interfaces . . . 9
  - 1.2.2 Surface Tension . . . 9
  - 1.2.3 Contact Angle . . . 10
  - 1.2.4 Young's Equation . . . 11
  - 1.2.5 Young-Laplace Equation . . . 11
  - 1.2.6 Vapour pressure and Kelvin equation . . . 12
- 1.3 Wenzel and Cassie Model . . . 12
- 1.4 Sliding Drops . . . 13
- 1.5 Superhydrophobic and Oleophobic Surfaces . . . 14

2 Theoretical Background **17**
- 2.1 Surfaces Preparation . . . 17
  - 2.1.1 Plasma Treatment . . . 17
  - 2.1.2 Chemical Vapour Deposition . . . 18
  - 2.1.3 Fluorination . . . 18
- 2.2 Scanning Microscopes . . . 19
- 2.3 Measuring Surface Tension . . . 20
- 2.4 Atomic Force Microscopy . . . 20
  - 2.4.1 Operating Modes . . . 21
  - 2.4.2 Droplet-Probe Force Measurements . . . 23
- 2.5 Spring Constant Calibration . . . 25
  - 2.5.1 Vertical Spring Constant . . . 25
  - 2.5.2 Lateral Spring Constant . . . 27
  - 2.5.3 Adhesion Force . . . 29
- 2.6 Laser Scanning Confocal Microscopy . . . 29
  - 2.6.1 Fluorescence Microscopy . . . 29
  - 2.6.2 Confocal Microscopy . . . 30
  - 2.6.3 AFM+Confocal . . . 31

3 Experimental Setup **33**
- 3.1 Surfaces Synthesis . . . 33
  - 3.1.1 Soot Template . . . 33
  - 3.1.2 Nanofilaments . . . 34
- 3.2 Droplet Probe . . . 35
  - 3.2.1 Cantilever Fluoranization . . . 35
- 3.3 AFM Measurements . . . 36
  - 3.3.1 Spring Constant and Deflection Sensitivity . . . 37

3.4 LFM . . . 37
3.5 Confocal Microscopy . . . 38
3.5.1 Setting and use . . . 38
3.5.2 Confocal Calibration . . . 39
3.5.3 Liquid and Dyeing . . . 39

4 Results and Analysis **43**
4.1 Surface Characterization . . . 43
4.1.1 SEM and AFM . . . 43
4.1.2 Contact Angle . . . 44
4.2 Adhesion Force . . . 45
4.2.1 Adhesion Measurement Imaging . . . 46
4.2.2 Low Quality Surfaces . . . 47
4.2.3 How Does Confocal Imaging Affect the Force Measurement? . . . 47
4.2.4 XZ Measurement . . . 48
4.2.5 Contact Angle . . . 51
4.2.6 3D Measurement . . . 53
4.3 Lateral Force . . . 55
4.3.1 Lateral Force Measurement Imaging . . . 56

5 Conclusions and Future Work **59**

Chapter 1

Introduction

Wetting is present everywhere and has a big influence in our daily life, due to this omnipresence the understanding of wetting phenomena has become mandatory for many fields in industry and science. In general, wetting occurs between a liquid and a surface, where drops can have different behaviour depending on the wetting properties of the surfaces. In industry we can find either hydrophilic and hydrophobic surfaces depending on the application. In this thesis we will focus the discussion to superhydrophobic surfaces.
Hydrophobic surfaces existed in nature even before their discovery, many organisms (plants, animal and fungus) have evolved to develop different liquid repellent properties, forming specific surfaces structures to repel water[1]. Superhydrophobic surfaces have been studied and synthesised in the last thirty years[2], inspired by many natural surfaces with hydrophobic properties, such as lotus flowers, roses and insect wings [3]. These surfaces present several properties of high interest for industry, such as self-cleaning [4], anti-biofouling[5], anti-icing [6], anti-fogging[3], lubrication [7] and more [8]. Wetting phenomena relevant in many fields, such as textile[9], automotive[10], and medical industry [11].

1.1 Motivations and Thesis Outline

Despite the advances in wetting phenomena and repellent surfaces, there are many challenges and open questions. Furthermore, industry demands better and cheaper synthesis methods [12]. Moreover, to develop high quality superamphiphobic surfaces the characterization is crucial. Standard characterization methods use optical macroscopic imaging and have several limitations[13]. Since super-repellent surfaces need micro- and nanoscopic texture, e.g., fractal or re-entrant roughness, in addition to low surface energy achieved by chemical passivation, the study of relevant length scales using micro-droplets is of utmost importance. Recent studies focus on the microscopic behaviour of superamphiphobic surfaces. In a recent study by Wong et al. [14], confocal microscopy and AFM force spectroscopy were used separately, revealing that the repellency of these surfaces may fail at microscopic and submicroscopic levels.
The aim of this study, inspired by the questions exposed above [15], is to measure the vertical and lateral forces of micro-sized droplets interacting with repellent surfaces. Previous publications have shown that is possible to use vertical and lateral forces on macroscopic drops to characterise surfaces, [16][17]. The ability of AFM to measure micro- to nano-Newton forces [18], can be used to scale-down vertical and lateral force measurement to the microscopic level[19]. The novel part of this research is to combine Laser Scanning Confocal Microscope(LSCM) with AFM to obtain visual information along with force measurements of micron-sized droplets. By implementing simultaneous confocal imaging and AFM force measurements, we will be able to compare these forces with the known models of capillarity and liquid-solid friction interaction. We will focus our interest in

superhydrophobic and supeamphiphobic surfaces, using liquids of different surface tension (ST). An important challenge that we will have to overcome, is to achieve stable micron-sized dyed droplets, i.e., that evaporate slow enough to image by LSCM.

The thesis chapters are organized as follows, in chapter 1, the main basic concepts about wetting and drop interaction will be discussed: surface tension, contact angle and capillary forces, which are of main interest for the experiments and a proper analysis.

Chapter 2, called ”Theoretical Background”, is mainly focused on the theoretical concepts regarding the experiments and the working of the equipment used, a brief explanation of the coating and knowledge for the surface preparation and characterization experiments, followed by an extensive description of the AFM. AFM has several working modes and functions that will be discussed in detail on this chapter, the principle behind LSCM also will be explained leading to the implementation of this two techniques together.

Chapter 3, we will show the procedures and experimental details. First we will show the steps for the surface synthesis its characterization. Then, by introducing the concept of droplet probe, the procedure for vertical and lateral force measurements will be explained. Finally, the experimental details for the implementation of LSCM will be discussed.

Chapter 4 will be focused on the results and analysis, first, the main characterization results of the repellent surfaces will be shown, then the force measurements without LSCM, the results of the first measurements with AFM-LSCM and finally the main results where both techniques are implemented. For the analysis, the image processing was made with python, facilitating the analysis. Finally the last chapter is for concluding and discuss the future work.

Finally, in Chapter 5 we will highlight the main conclusions and outlook of this theses.

1.2 Droplet Interface Interactions

1.2.1 Interfaces

An interface can be defined as the space or area separating two phases, likewise, a phase is a zone or volume of space where all the chemical and physical properties of a material are uniform[20]. The study of interfaces is of utmost importance for the understanding of many interactions at nanoscopic and microscopic level. It can be studied from different approaches depending on the field of study. An interface doesn't have to involve different states, there are interfaces between liquids and liquids, solid in liquids and so on, the only combination that is not possible is a gas-gas interface since gases tend to mix.
In this work we will focus on the wetting phenomena, especially on capillary forces and drop interaction with superamphiphobic surfaces, therefore the phases involved are three, solid (the repellent surfaces), liquid (drops) and gaseous (air). When we evaluate the drop interaction phenomena, the three phases involved meet in the three-phase contact line, which is crucial to describe the wetting phenomena. The liquid-air and liquid-solid interfaces are also important to understand the wetting and the forces involved.

1.2.2 Surface Tension

Surface tension (ST) is the main physical quantity to understand wetting phenomena and drop interaction[21], due to ST we have different liquid geometries, forces and thus different liquid behaviour. To have a further understanding of this property, first we need to define it using these two approaches:

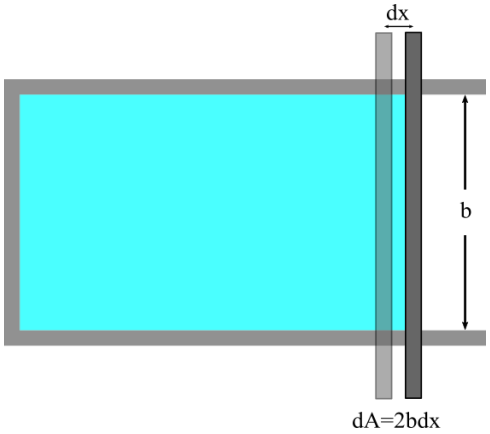

Figure 1.1: Scheme of the mechanical ST explanation, the blue colored square represent the bidimensional liquid. The rod can move in the x direction, then any change in the area is related to the rod displacement by $\Delta A = 2b \cdot \Delta x$.

Mechanical Approach

We can define the ST by looking at the work dW that has to be done by the rod(Fig.1.1) to increase the surface of a bidimensional liquid by an infinitely small amount of area dA, then the relation between the work and the energy γ is defined as the ST[20].

$$dW = \gamma \cdot dA \tag{1.1}$$

If we look at the force due to the movement of the rod, the change in the surface if we consider that the liquid has two faces(upper and lower surfaces) is $dA = 2b \cdot dx$, then we express the force in function

of the work:

$$F = \frac{dW}{dx} = -2\gamma b \tag{1.2}$$

Since the force is in the opposite direction of the change in x, it's negative. Here the ST relates the force on the "contact line" with the rod $\gamma = |F|/2b$.

Molecular Approach

To have a deeper understanding of the ST, we can take a look on the molecular structure of the liquid, and thus make a thermodynamic definition of it.

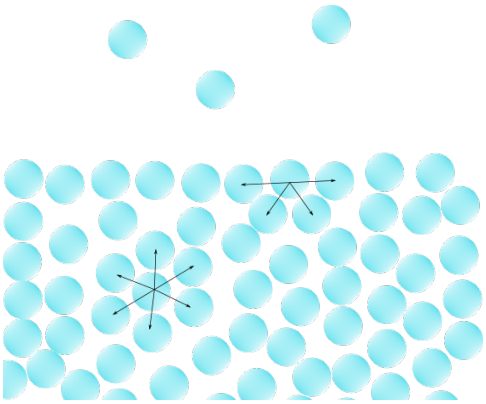

Figure 1.2: Scheme of a liquid-gas interface.

It's well known that in the liquid phase, the molecules attract each other due to hydrogen bonds or Van der Waals forces. For a single molecula within the bulk liquid, the number of neighbor molecules will be the most favorable energetically, nevertheless for the molecules on the surface, the number of bonds will be less than the ones deep into the liquid as shown in the fig 1.2. To bring a molecule from inside to the surface of the liquid (and thus change the liquid surface) work has to be done, this work causes the surface tension.

1.2.3 Contact Angle

The simplest way to quantify the wetting of a liquid on a surface is to measure the contact angle (CA)[21]. When we put a drop on a surface, the shape of it will change according to the surface tension of the liquid, but also to the energy of the surface. In wetting experiments, the three phase interface between the liquid, solid and air is also called contact line, where the liquid and the surface will form an angle (Fig.1.3). Depending on the wetting state of the liquid, we will call this angle contact angle (CA), in general, we will use this CA to have an idea of the wetting properties of the solid interacting with a particular liquid, since the liquid will have the same behaviour with the surface, the CA will be the same with a small dispersion and we can characterise the surface using this number.

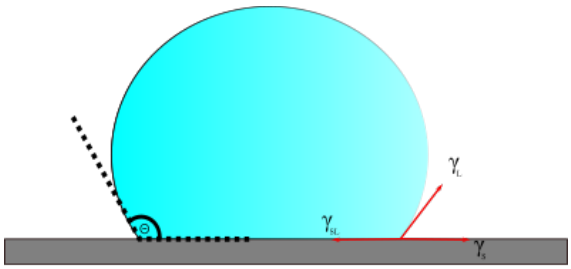

Figure 1.3: Representation of a drop lying on a surface, in the left side the contact angle (Θ) is shown, in the right side, the interface tensions that are present at the contact line.

1.2.4 Young's Equation

We know that for a liquid drop on a surface, the contact angle quantify the wetting interaction of the liquid on the solid surface. For total wetting we have CA$= 0$ then the liquid does not have a drop shape, but a puddle. In the case where CA> 0, the liquid have a drop shape and the contact angle will depend on the equilibrium between the spreading force between the liquid and solid and the ST contribution. To understand this equilibrium of forces, Young proposed a model where we consider the three different interfacial tensions in the contact line[22]:
The solid-vapor interface γ_S, the surface tension γ_L and the surface liquid interface γ_{SL}. Looking at the figure 1.3 we can make a balance of this tensions, but for the ST we need to consider the horizontal contribution, then we get the equation 1.3 relating this interfacial tensions with the CA. When the solid-vapor interface is higher than the solid liquid interface we can notice that the term $\gamma_L \cos\Theta$ is positive, this mean that the CA is in the range $0 < \Theta < 90^o$. In the opposite case, the term $\gamma_L \cos\Theta$ is negative and thus the CA should be higher than 90^o.

$$\gamma_L \cos\Theta = \gamma_S - \gamma_{SL} \tag{1.3}$$

Although this formula gives us a good idea of the liquid solid behaviour, in practice is not accurate. This is because the surfaces are not perfect and uniform, the roughness and heterogeneity have an influence in the wetting phenomena[[23].

1.2.5 Young-Laplace Equation

As the ST tends to minimize the surface, when a liquid is not in a container, we could expect to see always a planar shape in the liquid on a solid (CA zero) . Nevertheless, in many cases we have a curvature and a $CA > 0$. This curvature is influenced by the solid-liquid interaction explained by the Young equation. Nevertheless the drops can have more shapes, to explain bubbles, meniscus and other geometries seen in liquids we need a further understanding of the surface behaviour. For curved interfaces we can appreciate that, since the liquid is in equilibrium, there is a different pressure between the two parts of the interface, we call this the Laplace pressure. The Laplace pressure provokes a curvature that could be positive or negative[20]. Equation 1.4 shows the relation between the curvature of the liquid and the Laplace pressure between the liquid and the environment when the liquid is in equilibrium. For example, for a drop we have positive curvature and thus positive pressure difference. The opposite case is for meniscus(Fig.1.4) and liquid bubbles, where we have a negative pressure difference and thus a negative curvature[20].

$$\Delta P = \gamma \cdot \left(\frac{1}{R_1} + \frac{1}{R_2} \right) \tag{1.4}$$

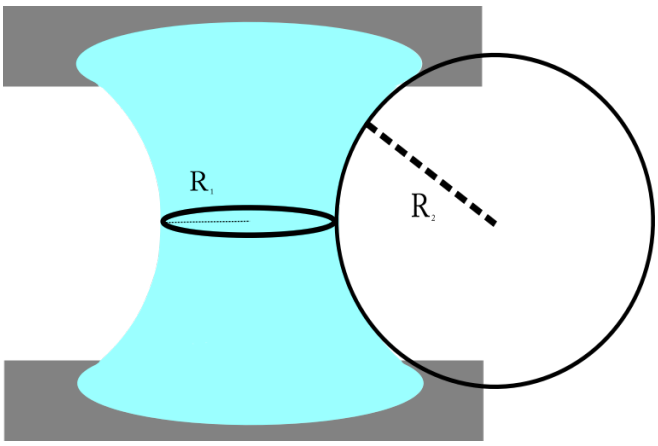

Figure 1.4: Representation of a liquid meniscus between two plates, in this example the two radius for the curvature are shown.

1.2.6 Vapour pressure and Kelvin equation

When a drop or meniscus shape is considered, the Laplace pressure also changes the vapour pressure of the liquid, making it more or less likely to evaporate depending of its curvature. To calculate the new vapour pressure we need to consider the initial pressure of the liquid P_0(planar liquid), the molar volume V_m , the ST γ_L and the curvature $1/R_1$ and $1/R_2$.

$$RT \cdot \ln \frac{P_o^k}{P_0} = \gamma V_m \cdot \left(\frac{1}{R_1} + \frac{1}{R_2} \right) \tag{1.5}$$

If we consider and spherical drop of radius r, we can simplify this calculation to the equation:

$$RT \cdot \ln \frac{P_0^k}{P_0} = \frac{2\gamma V_m}{r} \quad \Rightarrow \quad \frac{P_0^k}{P_0} = e^{\frac{2\gamma V_m}{RTr}} \tag{1.6}$$

Liquid	Surface Tension mN/m	$P_0(Pa)$	P_0^k/P_0
Watter	72.25	3169	1.001
Glycerol	59.4	0.01	1.0002
Ionic Liquid [24]	30	$\ll 0.1$	1.01
n-Hexadecane	29.32	20.2	1.003

Table 1.1: Vapour pressure of different liquids at $25°$, and relation P_0^k/P_0 considering an spherical drop of radius $r = 1\mu m$

In the Table 1.1 different liquids are shown, each one with its corresponding ST, the normal vapour pressure and the relation P_0^k/P_0.

1.3 Wenzel and Cassie Model

When it comes to superhydrophobic natural surfaces, the roughness and the topography of the surface is determinant for the hydrophobic behaviour, fractal morphology or reentrant roughness have shown an important influence in the hydrophobicity of the surface[25][26]. Hereafter, we show two models that have been proposed to describe this phenomena.

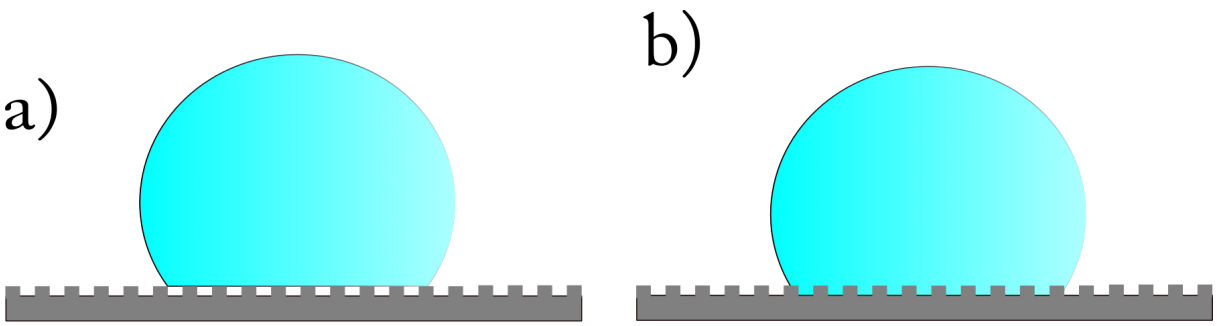

Figure 1.5: a) Drop in the Cassie state, the drop doesn't touch the lower part of the pillars, then the drop is in contact with two different materials, the air and the solid. b) Drop in Wenzel State, the drop is totally in contact with the surface.

Cassie Equation

The Cassie model states that, for a chemically heterogeneous surface (phases), the actual CA is an average of the contribution of the different CA (Θ_i) of the surfaces involved (equation 1.7)[27]. The most common case of Cassie state is when the two phases involved are a solid phase(for example nanofilaments) and gas phase(air), this is the case for many hydrophobic artificial and natural [28] surfaces.

$$\cos\Theta_{app} = f_1 \cos\Theta_1 + f_2 \cos\Theta_2 \tag{1.7}$$

Wenzel Equation

Wenzel model [29] considers the roughness of the surface and the increase of the surface area to explain the behaviour of a drop in rough surfaces, we define the Apparent CA as the CA observed in a macroscopic view. As shown in the equation 1.9 the apparent CA is related to the CA of the surface by the ratio R_{rough} defined in equation 1.8. This ratio is always more than 1, so the Apparent CA can be bigger for smooth surfaces and smaller for rough surfaces.

$$R_{rough} = \frac{\text{actual surface}}{\text{geometric surface}} \tag{1.8}$$

$$\cos\Theta_{app} = R_{rough} \cdot \cos\Theta \tag{1.9}$$

1.4 Sliding Drops

When drops are small enough, gravity does not have a big influence on the shape of a drop[reference]. But what happens when we apply a lateral force to a drop? A simple experiment is to place the drop on a tilted plane so the gravity is not normal to the surface, then we see a hysteresis of the CA. The hysteresis is defined as the difference between the advancing CA Θ_{Ad} and receding CA Θ_R.Depending on the wetting state, the drop can slide or not, depending on a threshold force that keep the drop attached to the surface [30]. This opens new ways to characterise the surface wetting properties [16]. The CA hysteresis is not provoked by the lateral force itself, but arises from a frictional force between the solid and the liquid, which depends on the wetting properties of the surface.

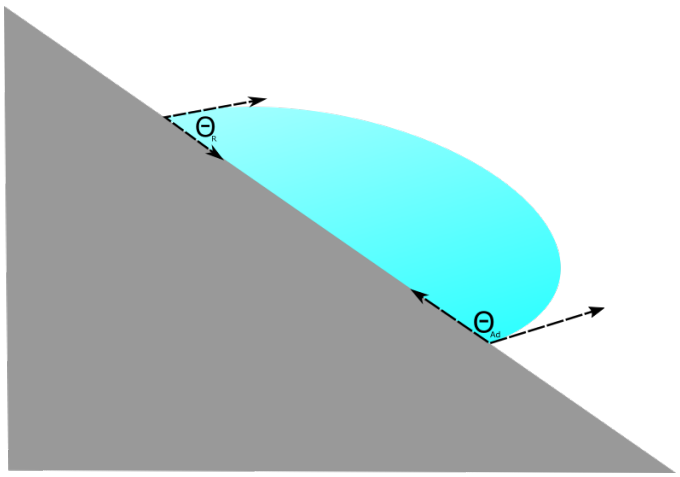

Figure 1.6: Drop sliding on a tilted plane.

Contact Angle Hysteresis and Frictional Forces

It is well know that the static contact angle does not give us all the information to characterise a surface[23], this is because measuring the contact angle has many experimental limitations and there is a lack of information, since the wetting interaction occurs in the micro and even in the nano-scale. As was we have seen before, for rough surfaces, drops can be in the Cassie state or Wenzel state, this can explain why there is an hysteresis in the contact angle as the drop slide on a surface.
Several experiments have shown that there is a relation between the dynamic friction force on a drop and the contact angle hysteresis on the contact line[31]. In equation 1.9 the lateral force depends on a experimental factor k that has been calculated between $1/2$ and $\pi/2$, the width of the drop (if we take Fig.1.6 as example, the width would be the length of the drop perpendicular to the plane of the image), the ST and the CA hysteresis. The greater the hysteresis, the more friction, if there is no hysteresis at all there are no frictional forces on the drop.

$$F_L = kL\gamma(\cos\Theta_{Re} - \cos\Theta_{Ad}) \tag{1.10}$$

Roll Off Angle

Roll off angle (RA) is a straightforward procedure to quantify the adhesion of the liquid and the surface, providing a further understanding of the wetting interaction. The surface rest on a leveled stage with a drop is placed on top of it, then by tilting the surface the drop will slice depending on its wetting state. We can separate the result in two kinds. When the RA is less than $90°$ we can have a quantitative result, associating the roll of angle with the wetting of the surface. On the other hand, when the angle of $90°$ is exceeded and there is no movement of the drop we cannot obtain a RA. One important step is to consider the static CA and the RA to make conclusions, for example, if the CA of a liquid is over $120°$ and there is no displacement, the drop is in Wenzel state.

1.5 Superhydrophobic and Oleophobic Surfaces

Hydrophobic surfaces have the property of repelling water, oleophobic surfaces repel organic liquids($\gamma = 27[\frac{N}{m}]$ for hexadecane) and amphiphobic surfaces can repel both liquids[32]. A surface is hydrophobic when the contact angle is over $90°$[33], superhydrophobic when the contact angle is over $150°$ [34], this definition apply for oleophobic and amphiphobic surfaces. To obtain superamphiphobic surfaces we need to consider the roughness of the surface and its surface energy. These magnitudes are indispensable to explain the interface interaction and quantify the wetting phenomena, in general

a hydrophobic surface can become oleophobic by decreasing the surface energy by applying a coating[35].
In this study, we will measure the adhesion of liquids interacting with two kind of superamphiphobic, transparent surfaces.
Nanofilaments: This surface is made of silicon filaments with 50-90 nm of diameter[36], by itself the morphology of this surface allow it to be superhydrophobic but, in order to have superamphiphobic behaviour, is necessary to decrease the energy of the surface[37]. This can be achieved making a coating of organosilicons.
Soot Template: To make soot template surface, a candle is placed under a glass slide to deposit a thin soot layer, this layer should be superhydrophobic due to its morphology. To improve the mechanical properties of the soot, a silica shell is made with CVD, this shell should has the same morphology but a different surface energy, the reentrant morphology of the soot with the low surface energy of the silica shell rends the surface superhydrophilic, to make the surface hydrophobic again an extra coating is necessary to decrease the surface energy[38], the result is a amphiphobic surface.

Chapter 2

Theoretical Background

2.1 Surfaces Preparation

The theoretical background for the understanding of the surface synthesis is presented. The principles for the nanofilaments and for the soot template surfaces are very different, nevertheless the aim of the fluorination is the same for both. The procedures and theory will be explained in general, and the implementation of these techniques will be discussed in the experimental section.

2.1.1 Plasma Treatment

Plasma treatment consists in using plasma to clean or (chemically) change surfaces, when gas is irradiated by UV light, generally O_2 or Ar, the electrons of the atoms excite to higher energy states, the atoms and molecules present ionise. During this work, the O_2 plasma treatment has two principal aims, the first is to clean the surface and the second is to activate the polymers (oxidation) surface before fluorination.

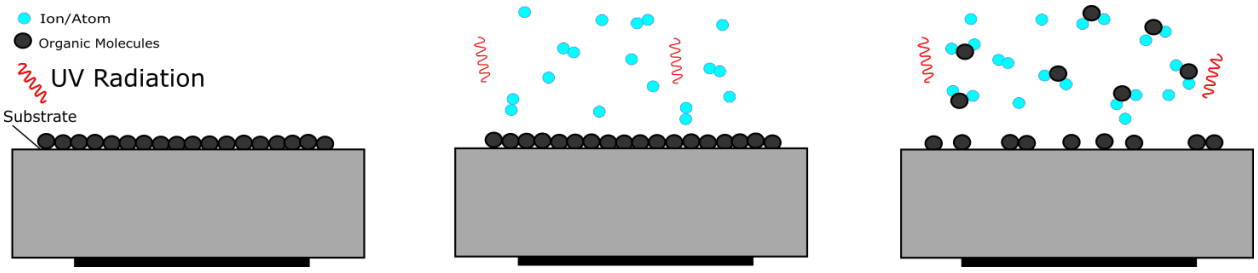

Figure 2.1: Schematic representation of the plasma cleaning process.

Plasma treatment is used to remove organic contamination, there are many mechanisms acting at the same time to remove the undesired molecules, electrons and ions will hit the molecules and detach them. The UV emission at low pressure breaks the organic bonds with the surface, in addition, the plasma activated atoms and the ionized molecules attach to the hydrocarbon molecules like H_2O and CO_2 making them more volatile[39].
For coating, plasma treatment can be used to ”activate” the surface by adding certain polar functional groups on the surface, increasing its wetting and facilitating the anchoring of different molecules for coating purposes.

2.1.2 Chemical Vapour Deposition

Chemical Vapour Deposition(CVD) is a widely used technique for coating and synthesis, although there are many kinds of CVD techniques, in this work, Gas-Phase Evaporation method is used. In the soot template surface, CVD is used for producing the silica shell[38] and for fluorination[40], the CVD fluorination is also used to reduce wetting on cantilevers.

2.1.3 Fluorination

As we saw in the introduction, many surface properties influence the wetting behaviour, if we have a hydrophobic surface we can improve its repellent properties by lowering the surface energy, to achieve this we can apply a coating of organosilicons (silanes)[41].
Several silanes can be used to change the surfaces wetting properties, in this study 1H,1H,2H,2H-perfluorodoctyltrichlorosilane(PFOTS) is used. The two methods for the fluorination process are described below.

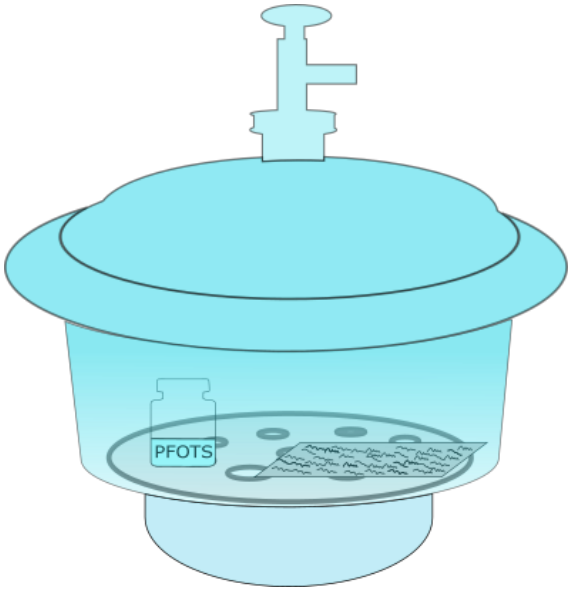

Figure 2.2: Scheme image of surface coating with PFOTS.

CVD Fluorination

By using a desiccator we can make an hydrophobic coating on the silica shell (figure 2.2). The first step is to break the bonds between the organylalkoxy group that involve the inorganic silane chains. Once the silica shell is activated with plasma, the hydroxyl groups formed in the silica shell receive the inorganic silica chains and the result is a coated surface with reduced surface energy[40].

Toluene Fluorination

To fluorinate Nanofilaments,first we need to make an O_2 plasma treatment to activate the surface, then we immerse them in dry toluene with PFDTS, the PFDTS molecules anchored onto the hydroxil groups on the nanofilaments surface and we obtain the coated surface[37].

2.2 Scanning Microscopes

Scanning Electron Microscope

Scanning Electron Microscope (SEM), unlike usual Optical Microscopes (OM), uses a beam of electrons instead of light [42], this has many advantages such as the implementation of Energy Dispersive X-ray Spectroscopy (EDS)[43], depending on the quality of the microscope. High resolutions SEMs can reach $1nm$ of resolution[44].
The beam of electrons is focused using condenser lenses, then the beam is deflected by coils to focus on sample. Scattered and backscattered electrons (SE and BE respectively) as shown in Figure 2.3. The microscope has a detector for each type of scattered electrons depending on the condition of the measurement. The collision of the electron beam with the electrons in the sample cause a change in the momentum of the sample electrons, this will generate a photon, specifically x ray photon.
Measured samples must be conductive or semi-conductive to avoid charging. As insulators don't release the collected charge from the beam of electrons, a gold coating must be applied to overcome this problem, in general Au is used.

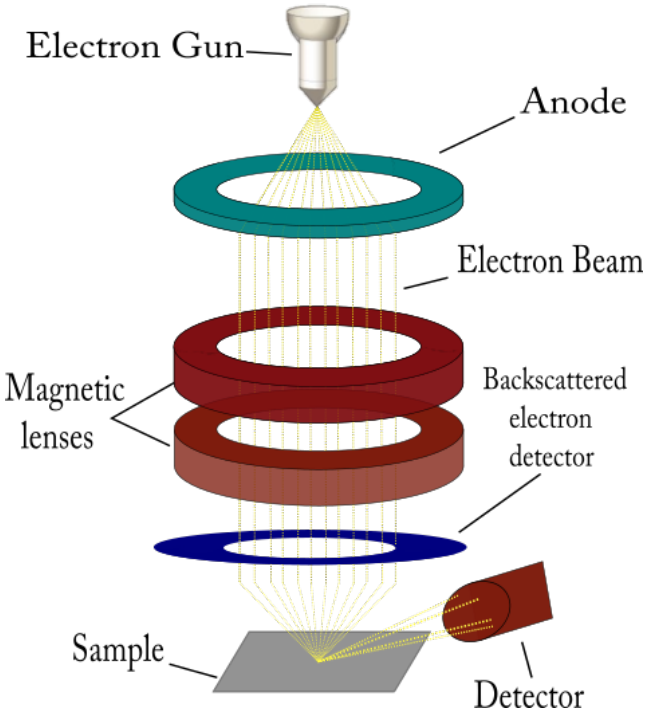

Figure 2.3: Scheme of the SEM functioning, the different components are shown. The anode attracts the electrons to form a beam, the magnetic lens direct focus the beam to scan the sample. The SEM is usually equipped with either a detector for electrons and back-scattered electrons

FIB

Focused Ion Beam (FIB) works in a similar way as the SEM[45], although instead of electrons, a beam of ions is used. FIB has several functions, such as imaging, deposition and etching. The source of the Ions is usually Gallium, the liquid Gallium wets a sharp Tungsten tip and then, by applying a electric field the beam of ionized atoms is emitted. The principal advantage of FIB is that we can remove material from different samples, while at the same time we image with SEM or FIB, depending on the sample requirements.

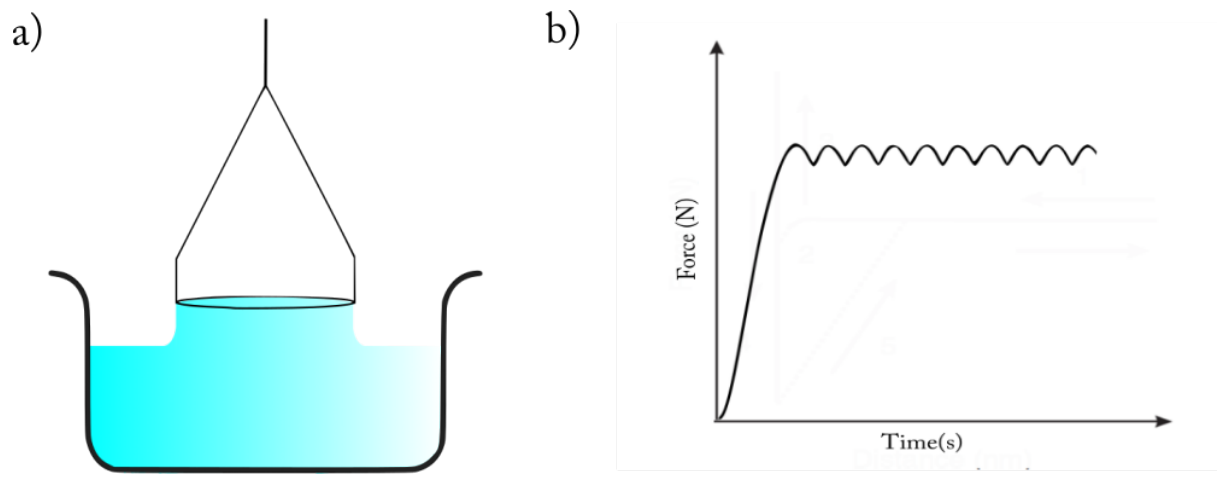

Figure 2.4: a) Du Noüy experiment, b) Force time graph, the force can be presented in grams or newtons depending on the calculation.

2.3 Measuring Surface Tension

For the surface tension measurements, a surface tensiometer (SFT) is implemented. A SFT consist of a hydrophilic probe interacting with the surface of the liquid(figure 2.4a). This device often has a variety of probes depending on the liquid composition and amount of liquid. In this case the probe is a platinum-iridium ring[46](Du-Noüy Tensiometer) that is immersed in the liquid and then lifted until the maximum force is reached. Once the software detects a maximum in the force, the probe is slightly submerged again and the process is repeated n number of iterations or until the probe and the liquid tear apart(figure 2.4 b). The force is recorded in the software and the average value of the maximum force is used to calculate the work necessary to break the surface tension, by knowing the shape of the probe, calculating the work is straightforward if we apply the corrected Du-Noüy model[47].
To calculate the ST, we need the total force acting on the ring P_T, the contribution of the ring weight P_{Ring} and the inner and outer radius R_i and R_a of the ring, using equation 2.1 we can calculate the ideal surface tension γ_0. Nevertheless, given that this equation refers to an ideal ring, we need to consider the experimental error and the contact line relaxation. If we want to have a more realistic result, we can introduce a correction factor f as shown in the equation 2.2.

$$P_T = P_{Ring} + 2\pi(R_i + R_a) \cdot \gamma_0 \tag{2.1}$$

$$\gamma = f \cdot \gamma_0 \tag{2.2}$$

2.4 Atomic Force Microscopy

Atomic Force Microscope (AFM) is one of a series of scanning probe microscopes (SPM) that have been created to overcome the barrier of the optical resolution limit[48]. AFM uses a micro-sized cantilever with a probe to scan surface with nanometric, in some cases atomic, resolution and to make force measurement with different settings and probes[49].
The AFM allow us to scan in 3 dimensions using Piezoelectric crystals. This cantilever, usually made of silicon, is irradiated with a laser beam to detect the deformation of the cantilever when it moves through a surface and the laser beam is deflected, this deflection is measured by a Position Sensitive Photodetector (PSD) that is able to detect the vertical and lateral deflection of the cantilever. The laser and the PSD have to be aligned as shown in Fig. 2.5. AFM measure changes in the height of the surface with a resolution of fractions of nanometers to Angstroms. To relate the virtual deflection(V) and the

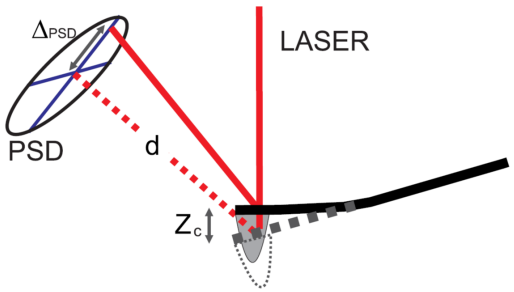

Figure 2.5: Ilustration of the sensing mechanism of the AFM, the laser idealy is alined in the center of the psd, Z_c represent the cantilever deflection.

cantilever deflection(Δz) we need to find the Deflection Sensitivity(γ), defined by the formula:

$$\Delta z = \gamma \Delta V. \tag{2.3}$$

By knowing the elastic properties of the cantilever, we can also calculate the force that is acting on the cantilever using its vertical deflection. For a cantilever the force is related with its deformation as shown in equation 2.4 where k is the elastic constant and Δz it's the cantilever deflection.

$$F = -k \cdot \Delta z \tag{2.4}$$

2.4.1 Operating Modes

Contact Mode Imaging

In contact mode, the cantilever tip statically scans the sample surface and its topography is recorded using the virtual deflection shifts measured on the PSD, to keep the deflection constant, the microscope changes the height of the cantilever and the system records this height. This kind of operation mode is used for surfaces that are not too rough, and low stiffness cantilevers must be used. Contact imaging can be very precise for flat surfaces, but has several problems for rough and soft surfaces, the constant contact between the surface and the tip make the tip susceptible to damage and contamination .

Intermittent Contact Mode

Intermittent Contact Mode, or AC mode uses the natural resonance frequency of the cantilever to detect the interaction of the tip and the surface, when the tip begins to interact with the the surface the cantilever will suffer a shift in the frequency or the amplitude, the PSD detects this change, adjusting the height of the cantilever. This method is often used to measure rough or smooth surfaces, as the interaction of the tip and the sample is minimum, both remain unaffected.

Force Spectroscopy

Force Spectroscopy is a very powerful and widely used technique of AFM. By approaching the cantilever against the surface and press it, we can record the vertical deflection as we apply a force on it. Using the stiffness of the cantilever it is possible to calculate the force that acts on the tip as a function of time (Fig. 2.6) or distance (Fig. 2.7).
In force spectroscopy, we have the position of the cantilever due to the piezoelectric crystals Z_p and the vertical deflection of the cantilever Z_c, by knowing these two quantities we can calculate the tip-surface distance $D = Z_p + Z_c$, the movement of the piezotranslators can be described by an arbitrary

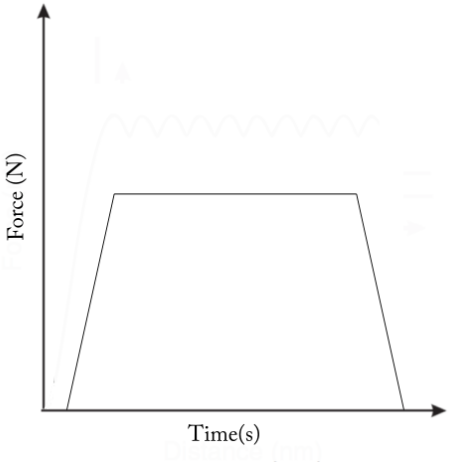

Figure 2.6: Force time curve, a setpoint force is reached and after a time the cantilever starts retracting.

function (force or distance versus time), generally a triangle or a trapezium function (figure 2.6), also there can be a trigger point in case the maximum force is reached before.
Depending on the probe and the surface nature, there can be different forces involved, the previous knowledge or notion of these forces is mandatory to select the correct cantilever, since its stiffness is inversely proportional to the sensitivity of the force measurement. For example, stiffer cantilevers are less sensible to capillary forces.

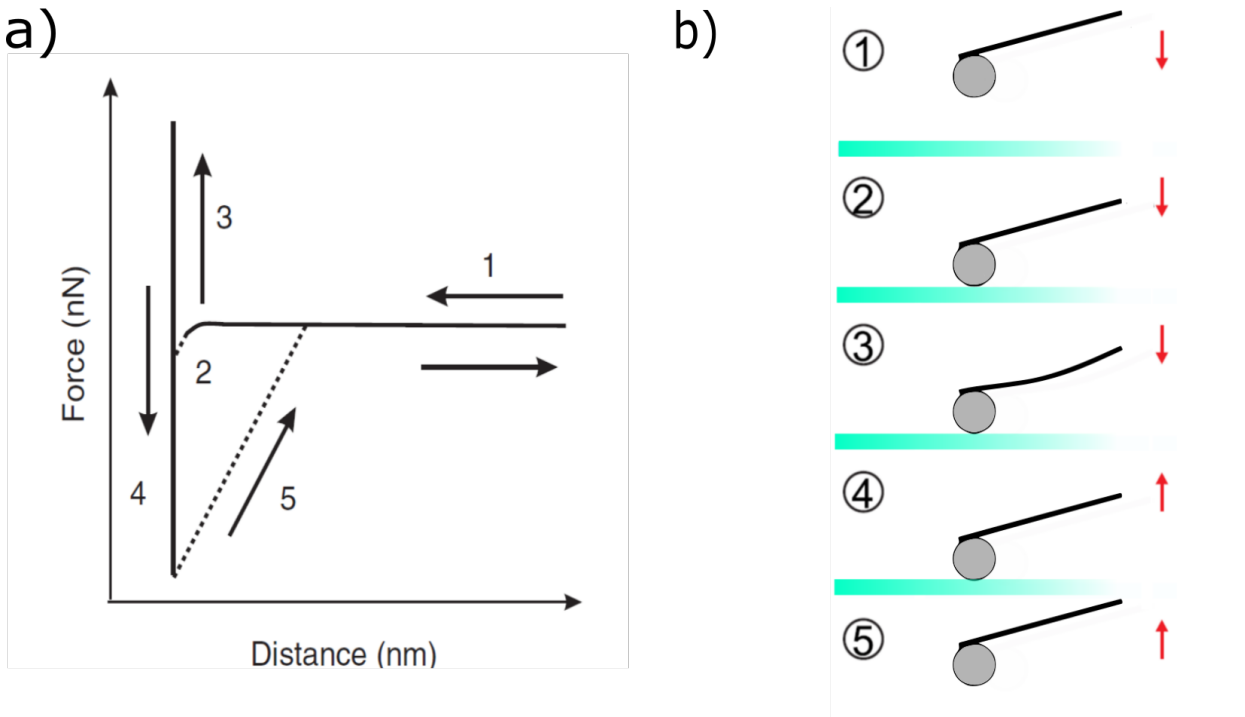

Figure 2.7: (a)Typical force measurement(b)Scheme of an drop-surface FM, we can see that we have the same behaviour of a tip probe FM, nevertheless the step in and the pull out forces show a different shape, this is due to the predominance of the capillary forces and pinning.

Typical Force Curve

The standard force measurement is often made using a cantilever with a solid probe (a tip or a colloid), the surface-probe interaction describe the surface quality and, depending on the surface, different tips

can be used, the stiffness of the cantilever is also relevant to have accurate results. In this kind of force measurement, most of the time we have the same behaviour, hence the same curve shape. We can recognize 5 moments of importance in a typical force curve.

- Zero force region: at this stage, the cantilever does not feel any force while it moves, we have a constant value of force as we change the distance.
- Snap-in: As the cantilever approach to the surface, it feels the attractive forces(Vab der Waals), the tip jumps to the surface.
- Constant compliance region:The tip is in contact with the surface, the force increases proportional as the cantilever distance decrease. The slope of the constant compliance relation will give information about the mechanical properties of the surface.
- Retract: After a certain time or after reaching the trigger point, the cantilever will star retracting, it also can have a linear relation with the force depending on the elastic properties of the material.
- Snap-out: When the cantilever loses contact with the surface it will stop feeling the attractive forces, jumping to the initial force value(zero), the attractive force can make the cantilever stay in contact with the forces after returning to the snap-in distance, provoking a deflection in the opposite side, this is why there is a gap between the snap-in and the pull-out distance.

Lateral Force Microscopy

As we can use the vertical deflection to measure normal force interaction, lateral deflection can be used to measure the torsion forces on the cantilever and thus calculate the friction force on the probe, either colloidal probes, droplets or tips(figure 2.8). As the vertical and lateral deflection signals are independent, we can measure both, height and lateral interaction in a single measurement. The main challenge of LFM is to calibrate the lateral deflection sensitivity and the torsion spring constant.

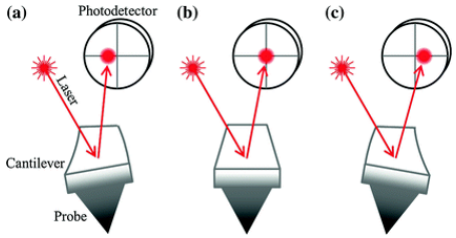

Figure 2.8: Scheme of a lateral force measurement, as the probe rubs the surface the PSD detect the lateral deflection, when the cantilever is calibrated we can record this deflection in Newtons.

2.4.2 Droplet-Probe Force Measurements

According to the forces to measure, we can use either tip or colloidal[50] probes, tip probes are usually used in imaging and to test mechanical properties, nevertheless colloidal probes are widely used for force measurement since they have many advantages[51]. Colloidal probes can have different composition and can be customized, for example liquid[52] or even cells[53]. Using drops instead of solid colloid leads to the measurement of the capillary interactions using drops with the surface[54]. Using a specific liquid composition we can attach a droplet to a cantilever[55] and make force measurements of the interaction between this microdroplet and the surfaces to investigate(fig 2.9). In order to avoid wetting on the cantilever, a fluorinated coating is required, a hydrophobic cantilever.

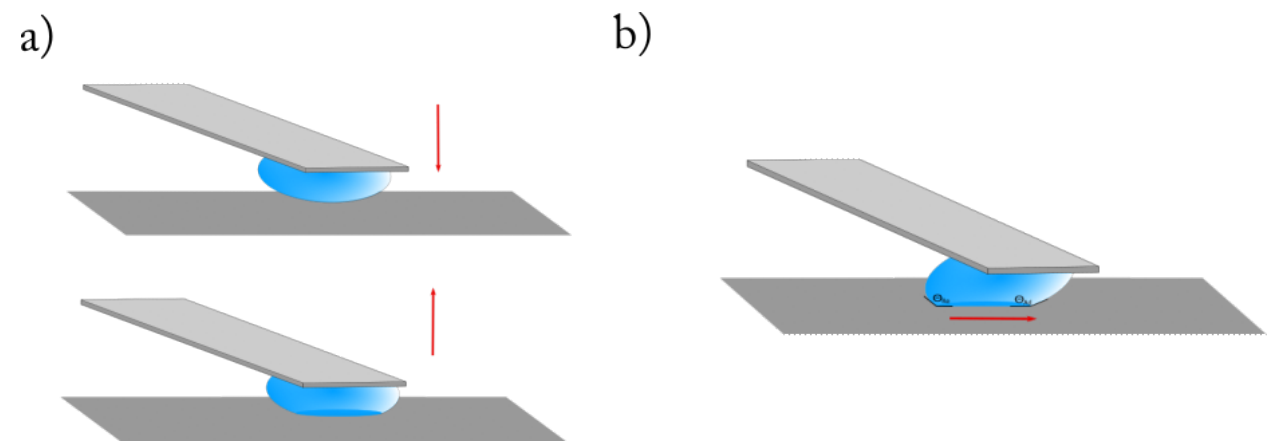

Figure 2.9: Illustration of the the droplet probe technique, this technique allows us to measure the drop-surface interaction forces with resolution of $[nN]$. We can perform two kind of experiments a)Normal Force measurement, we measure the vertical force on the cantilever as we retract the cantilever. b) Friction force measurement, we can calculate the lateral forces as the drop displaces on the surface.

Drop-surface Force Curve

In most force curves, when using tips and probes there are capillary forces, nevertheless it is negligible in comparison and often ignored since the other interactions are more relevant, this is why for tip and colloid probes measuring solid-solid interactions, the curves tend to be similar in behaviour. Droplet-

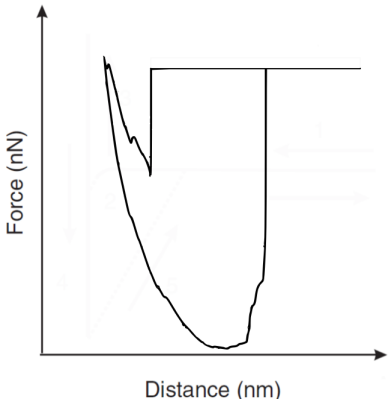

Figure 2.10: Force Curve of a drop probe force spectroscopy, as the capillary forces rules the interaction, we don't have the force curve of a typical force spectroscopy, nevertheless the steps are still the same.

probe force spectroscopy, capillary force has the main role and the force curve changes considerably, we can recognise five steps as in the typical force curve, with a few differences. The snap-in is bigger, because when the drop contacts the surface it spreads and the drop changes its shape to minimize the energy, this snap-in is bigger if the surface is more hydrophobic. The approaching and receding in contact force behaviour depends on many factors, the trigger point, the drop composition and the pinning with the surface. The pinning cause smalls jumps in the force value because the pinning area loses contact partially, when the retracting force is too much we have the pullout, but this is not the maximum value of the capillary force. After the pull out, the drop doesn't feel more forces. The minimum force recorded by the AFM should correspond to the adhesion force due to capillary force of the drop, the surface and the tip.

2.5 Spring Constant Calibration

As we have seen above, the spring constant is necessary to measure normal and lateral force, and there are several methods to calculate the spring constant. Here we will focus on the ones we will use in the experiments. Before we go further on these methods it is important to know the three spring constants present in the cantilever.
We have a spring constant for the lateral and the normal displacement Δx and Δz respectively. As we see in equation 2.5 the normal k_N and lateral k_L spring constants relate the displacement with the force. There is a third spring constant k_T that relate the torque acting on the cantilever to the torsion angle ϕ.

$$\begin{aligned} F_N &= k_N \cdot \Delta z \\ F_L &= k_L \cdot \Delta x \\ \tau &= k_\phi \cdot \phi \end{aligned} \tag{2.5}$$

2.5.1 Vertical Spring Constant

The Vertical Spring constant is the most important one, since the vertical force spectroscopy is widely used and have become a standard procedure to measure microscopic interaction forces and to measure mechanical properties on different surfaces.
There are several methods to measure the vertical spring constant, the most relevant for this work will be described below[56].

Beam Theory

Euler-Bernoulli Beam Theory gives us a way to calculate the spring constant using the elastic properties and the dimensions of the cantilever. The bending of the cantilever causes the virtual deflection, using the deflection sensibility we can have the actual value of the spring constant. The quantity $\frac{Z_c}{dz}$ represents the slope of the laser position vs the cantilever position. The equation 2.6 relates this quantity with the Young's Modulus E, the width b, the length l, the thickness t_c and the force f that is acting on that point.

$$\frac{dZ_c}{dz} = \frac{6fl^2}{Ebt_c^3} \tag{2.6}$$

Using the fact that, at the tip position, $x \approx l$ and this implies that the slope is $\frac{Z_c}{l}$, using the fact that $F = Z_c \cdot k_c$, where k_c is the spring constant lead to the equation:

$$k_c = \frac{Ebt_c^3}{4l^3} \tag{2.7}$$

This method is very accurate, nevertheless it is not easy to obtain the dimensions of the cantilever without using equipment like SEM or LSCM.

Thermal Method

The molecules in the environment interact with the cantilever and cause vibrations, this thermal noise can be quantified in terms of the temperature, obeying the equipartition theorem, we can pose the relation:

$$\frac{1}{2}k_N \left\langle z^2 \right\rangle = \frac{1}{2}k_B \cdot T, \tag{2.8}$$

where $\langle z^2 \rangle$ represent the mean square value of z displacement, K_b is the Boltzmann constant and T is the temperature. We can express the spring constant in terms of:

$$k_N = \frac{k_B \cdot T}{\langle z^2 \rangle} \tag{2.9}$$

So far we just need the mean square virtual deflection and with the deflection sensitivity the calculation of $\langle z^2 \rangle$is straightforward.

Sader Method

To understand the Sader method, we need to assume the cantilever as a thin plate, which is slightly deflected, these small deflections(w) are ruled by the equation 2.10, where the plate is in the plane x, y, and ω is the deflection on the cantilever:

$$D\nabla^4 w(x,y,t) + \sigma \frac{\partial^2 w(x,y,t)}{\partial t^2} = q(x,y,t) \tag{2.10}$$

where $D = Eh^3/(12(1-\nu^2))$ is called flexural rigidity, E is the Young modulus, the Poisson ratio ν, t_c the thickness of the cantilever, σ the mass per area and q is the external transverse loading per area. The solution to this equation is not straight forward, we can propose a solution using the resonance frequency of the cantilever f_R in the form:

$$w(x,y,z) = W(x,y)\cos f_R t \tag{2.11}$$

then we have a function in terms of the resonance frequency, to obtain a solution for the cantilever deflection some corrections must be considered, such as, the loading needs to be considered, and the damping with the air. As the aim of this work is not to solve this problem we let to the reader the references [57][58]. After considering all this corrections we can numerically obtain a solution of the form:

$$k_z = 0.1906 \rho_{fluid} b^2 l Q_f f_R^2 \Gamma_i^f(f_R) \tag{2.12}$$

where ρ_{fluid} is the density of the fluid, Q_f is the Quality factor of the resonant peak and $\Gamma_i^f(f_R)$ is the imaginary component of the hydrodynamic function described by Sader in eq (20) of the reference [57].

Vertical Deflection Sensitivity

Usually, when we need the vertical deflection sensitivity, we can use a simple force measurement to calculate it, using the known movement of the piezo and the deflection recorded on the movement, then the slope between this two quantities give us the sensitivity with a straightforward calculation (as long as the calibration sample is not significantly deformed).
As with the Sader method, we can use the natural frequency of the cantilever to calculate the sensitivity, this advantageous for many purposes, but the main reason is to keep the tip without damage or contamination. To understand this process, first we need to define the power response function $S(f)$ of a harmonic oscillator. As the name of the function says,in equation 2.13, we can appreciate the behaviour of the oscillator at different frequencies f, using the resonant frequency f_R the quality factor Q and the dc power response P_{dc}.

$$S(f) \cong P_{white} + \frac{P_{dc} f_R^4}{(f^2 - f_R^2)^2 + \frac{f^2 f_R^2}{Q^2}} \tag{2.13}$$

When we integrate $S(f)$ over all the frequencies(equation 2.14) we obtain the average voltage of registered on the PSD.

$$\langle V^2 \rangle = \int_0^\infty S(f) df \tag{2.14}$$

Then by solving this and using $\langle z \rangle = \gamma \cdot \langle V \rangle$ we obtain the equation:

$$\langle z^2 \rangle = \frac{\pi}{2} \gamma^2 f_R P_{dc} Q \tag{2.15}$$

But we want to obtain the value γ, and we can't measure directly $\langle z \rangle$, to solve this we use the equipartition theorem for an harmonic oscillator from equation 2.8. Then we have the final expression for the sensitivity.

$$\gamma = \sqrt{\frac{2 k_B T}{\pi k f_R P_{dc} Q}} \tag{2.16}$$

2.5.2 Lateral Spring Constant

In LFM, there are two spring constants involved, this makes the cantilever calibration more challenging. In general, this kind of measurement uses a colloidal probe to measure the lateral force, tips can be used depending on the surfaces properties and the kind of interaction producing the friction. Most of the methods to obtain the normal spring constant can be adapted to the torsional k_ϕ, in this section we will describe the lateral Sader method.

Sader Method

The Lateral Sader method[59] uses the same principle for finding the normal spring constant, starting with the equation to describe the deflection angle ϕ, where ρ_c is the density of the cantilever, I_p is the polar moment of inertia, G is the shear modulus of the cantilever, K is the geometric function of the cross section and the function m is the applied torque:

$$\frac{GK}{l^2}\frac{\partial^2\phi(x,t)}{\partial^2} - \rho_c I_p \frac{\partial^2\phi(x,t)}{\partial t^2} = m(x,t) \tag{2.17}$$

Just as in the normal case, we use the Fourier transform to solve this equation obtaining the spring constant k_phi:

$$k_\phi = \frac{1}{3\pi^2}\rho_c b^3 t_c l \omega_{t,vac}^2 \tag{2.18}$$

where:

$$\omega_{t,vac} = f_t\left(1 + \frac{3\pi\rho b}{2\rho_c h}\Gamma_r^t(f_t)\right) \tag{2.19}$$

The final component to obtain the final expression of k_ϕ is the relation, where Q_t is the torsional resonance quality factor:

$$\rho_c t_c = \frac{3\pi\rho_{fluid} b}{2}[Q_t\Gamma_i^t(f_t) - \Gamma_r^t(f_t)] \tag{2.20}$$

Finally, the spring constant is expressed as:

$$k_\phi = 0.1592\rho_{fluid} b^4 l Q_t f_t^2 \Gamma_i^t(f_t) \tag{2.21}$$

Now that we have the ”angular” spring constant, to obtain the torsional spring k_L, we just need to know the arm length(r).

$$k_L = r \cdot k_\phi \tag{2.22}$$

Lateral Deflection Sensitivity

As for the normal case, we can define the torsional deflection sensitivity that relates the change in the angle ϕ with the lateral virtual deflection V_L:

$$\phi = \gamma_\phi \Delta V_L, \tag{2.23}$$

We can use the equipartition theorem (equation 2.17) to express the lateral deflection sensitivity in terms of $\langle V_L \rangle$:

$$\frac{1}{2}k_B T = \frac{1}{2}k_\phi \left\langle \phi^2 \right\rangle, \tag{2.24}$$

$$\gamma_\phi = \sqrt{\frac{k_B T}{k_\phi \langle V_L^2 \rangle}} \tag{2.25}$$

Now, following the same procedure used for the normal sensitivity, since the lateral movement can be reduced to a simple harmonic oscillator, we just need to record the power response and fit S(f) for the lateral deflection, and use the relation:

$$\gamma_\phi = \sqrt{\frac{2k_B T}{\pi k_\phi f_t P_{dc} Q}} \tag{2.26}$$

Now that we have the polar sensitivity, to obtain the torsional sensitivity γ_L, we just need to know the arm length.

$$\gamma_L = r \cdot \gamma_\phi \tag{2.27}$$

2.5.3 Adhesion Force

We can find the capillary force the normal force measurement experiment, we need to consider the forces all involved in the experiment[19]. The two main components are due to the surface tension and the Laplace pressure. As we can see in the figure 2.11 if we take a component dl of the contact line, the force dF will form an angle θ with the surface, so the contribution to the adhesion force should correspond to the vertical component of this force, then we just have to integrate over the contact line, if we consider it as a circle of radius "r" then the force due to ST is $2\pi r\gamma \sin\theta$. To obtain the Laplace pressure contribution, we just need the pinning area of the drop, for a circle this area A correspond to πr^2.

$$F_{adh} = -2\pi\gamma r \sin\theta + \pi r^2 \Delta P \tag{2.28}$$

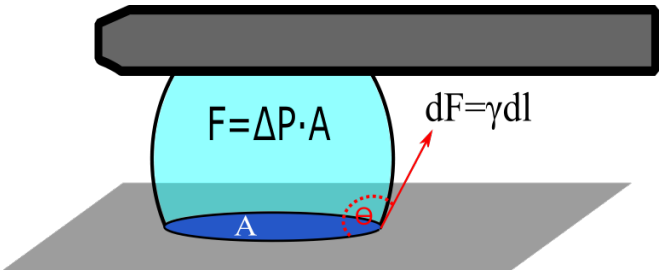

Figure 2.11: Drop force experiment representation, the two forces component are shown.

2.6 Laser Scanning Confocal Microscopy

Laser Scanning Confocal Microscopy (LSCM) is one of the main techniques used in combination with droplet probe force spectroscopy, for the understanding how this microscope works, we need to introduce the concepts of fluorescence and fluorescence microscopy. LSCM was created to solve the problems and limitations of the fluorescence microscope[60].

2.6.1 Fluorescence Microscopy

Fluorescence is a type of luminescence that occurs due to particles excitation. In Fluorescence Microscopy (FM), a dyed sample is irradiated by a external monochromatic light source, the dye consist in molecules whose electrons absorb energy and turn in to an excited state, after this, the electrons release that energy and go to their corresponding ground state by emitting photons, generally with less energy than the original radiation due to Stoke's shift. This phenomenon was first used in microscopy in the 1930s, the main advantages of the FM is the detection of small regions or sections of the samples controlling the dye process, for example in biology it is often used to dye proteins or particular tissues. By using a beam splitter, the light from the monochromatic source is filtered and just the emitted light from the fluorescence reaches the detector(Fig. 2.12). There is a wide range of dyes for FM imaging, the main difference correspond to the wavelength of excitement of the dye, this will depend on the monochromatic light source used. The dyes can also have different chemical composition and behaviour, for example hidrophobic or hidrophilic dyes will be used depending on the sample. Functionalised dyes can be used to emit light depending on the PH or other chemical interactions, specific dyes can also be used for live cell imaging.

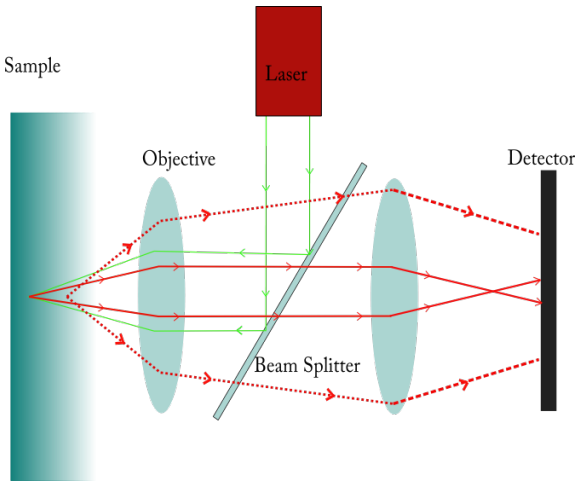

Figure 2.12: Schematic FM functioning.

2.6.2 Confocal Microscopy

Laser Scanning Confocal Microscope(LSCM) was invented in 1955 by Marvin Minsky[60], to overcome the limitations of FM. Besides far surpassing its predecessor, LSCM has evolved to become a powerful imaging tool, able to scan different optical planes, making 3D structures. LSCM is able to reach hundreds of nanometers of resolution depending on the configuration.
LSCM uses the same principle as FM, but instead of detecting the light directly from the lens, we have a pinhole to avoid the out of focus light. This leads to the problem that we can only see one spot at the time. To solve this it is necessary to scan the sample, by moving the sample or moving the beam, the last method is the most, allowing to make fast imaging and avoid undesired vibrations on the sample. Just as in the case of FM, the LSCM is widely used in biology, at different scales, nevertheless for the study of wetting interaction LSCM has become an important tool to visualize the wetting interaction at macroscopic and microscopic level[ref].

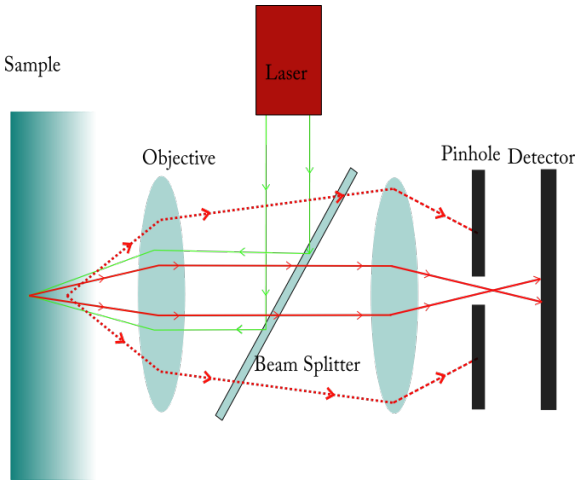

Figure 2.13: Working principle behind LSCM, the difference between this microscope and FM in the scheme is the pinhole, nevertheless, it is important to know that the confocal also has the scanning components, that moves the laser or the sample, usually with piezo components.

2.6.3 AFM+Confocal

The confocal setup(Fig. 2.11) allows us to place an AFM head over the objective, and thus been able to image the AFM force measurements. For LFM implementing LSCM, the surfaces most be

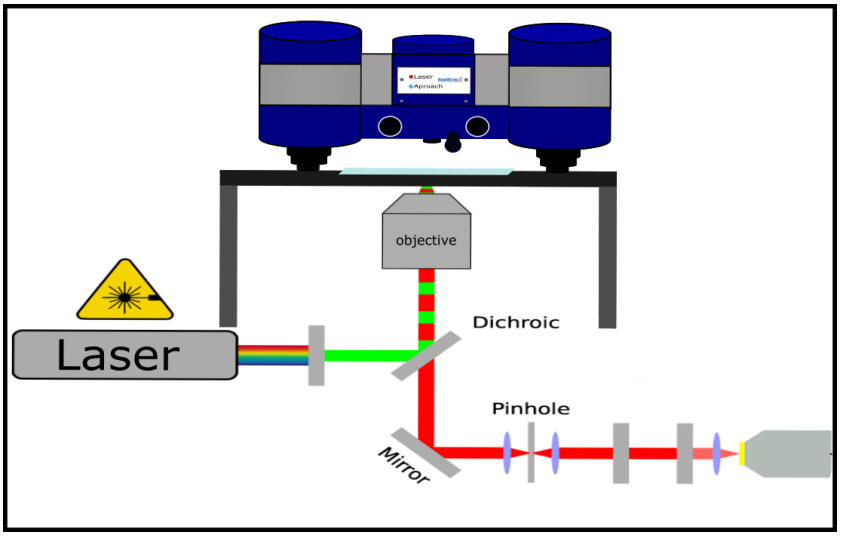

Figure 2.14: Schematic representation of the confocal setup, combined with AFM.

more transparent than the experiments showed before, since the speed of movement of the cantilever doesn't allow to take detailed images, more transparent surface improve the quality of the image considerably, this is why we do not use superamphiphobic surfaces, but superhydrophobic surfaces. This is also convenient because we want to see a contact angle hysteresis and a strong interaction with the surface will allow us to observe this more easily.

Chapter 3

Experimental Setup

In this chapter the experimental settings and procedures will be described. The principal characteristics and operation of the AFM will be discussed, and the procedure to attach a liquid droplet in the end of a tipless AFM cantilever probe. The surface preparation of superhydrophobic samples will also be presented.
For the confocal imaging experiment, a handmade LSCM was implemented, the functioning and operation of the microscope will be discussed int he following sections. The composition of the liquid for confocal imaging will be described, as well as the procedure to dye the liquid.

3.1 Surfaces Synthesis

In the following section, the experimental setup and procedure for the synthesis of superamphiphobic surfaces will be presented, for both soot and nanofilament surfaces, the procedure is the same for all glass slides, we use high precision glass slides for confocal imaging.

3.1.1 Soot Template

To make soot template surfaces, we subject the slides to different processes, which are described bt Deng et al. [38]:

- Cleaning: To clean the glass slides it is necessary to immerse them in a glass recipient with toluene, ethanol and acetone, respectively, and apply a sonic bath for 5 minutes each. After this is necessary to dry the slides in an oven at $60°C$ for 1 hour under 100 $[mbar]$.
- Plasma cleaning: In order to remove any contamination remnant, the glass slides must be introduced in the plasma cleaner for 5 minutes at 100% of capacity.
- Soot layer: This step is made with a candle, the clean slides go over the candle flame and the soot is deposited over the slide surface, a homogeneous soot layer is reached after 40 seconds of exposition to the flame.
- Silica Shell: The slides go in to the desiccator, with 3ml of tetraethoxysilane and 3ml of NH3.
- Calcination: In order to make the surface transparent, we need to get rid of the soot, this can be achieved by depositing the samples in an oven at $500°$C for 5 hours, the silica shell is not affected during this procedure.
- Fluoranization: The silica shell with the soot topography is enough for superhydrophobicity behaviour, nevertheless, in order to have a superolephobic surface it is necessary to decrease the surface energy, to achieve this we put the surfaces in a desiccator with $100\mu L$ Trichloroperfluoroctylsilane at $50[mbar]$ for 1 hour.

3.1.2 Nanofilaments

The steps for the nanofilaments are as follows [36]:

- Solvent cleaning: This process is the same as for the soot template.
- Plasma cleaning: This process is the same as for the soot template.
- Nanofilaments synthesis: For this process we prepare 100 ml of toluene with $150 - 170[ppm]$ with $0.4[ml]$ of trichloromethylsilane in a container and stir, then we introduce the slides in the solution for 3 or 4 hours, in this time the siynthesis occurs. After this time the surfaces are cleaned in toluene. At this point the surfaces should be superhydrophobic, but in order to obtain superoleophobic surfaces we need to apply the fluorination.
- Plasma Activation: For the next step is necessary to activate the surface with plasma, we insert the surfaces in the plasma at 40% power for 2 minutes.
- Fluoranization: We prepare 100ml of hexane with $100\mu l$ trichloroperfluordecylsilane and stir. Immerse the surfaces in the solution for 1 to 2 hours. After this procedure the surface is cleaned in hexane.

Goniometer

The Goniometer setup (figure 3.1) consist in a level stage to place the surface to characterize, from the software the stage can move in 3 dimensions and also can rotate as required. The system has a syringe that can be controlled by the software, by knowing the model of the syringe we can control the exact amount of liquid deposited on the surfaces. With the camera the shape of the drop can be captured and then analysed with software. The illumination is important for obtaining a high contrast and track the drop edge.

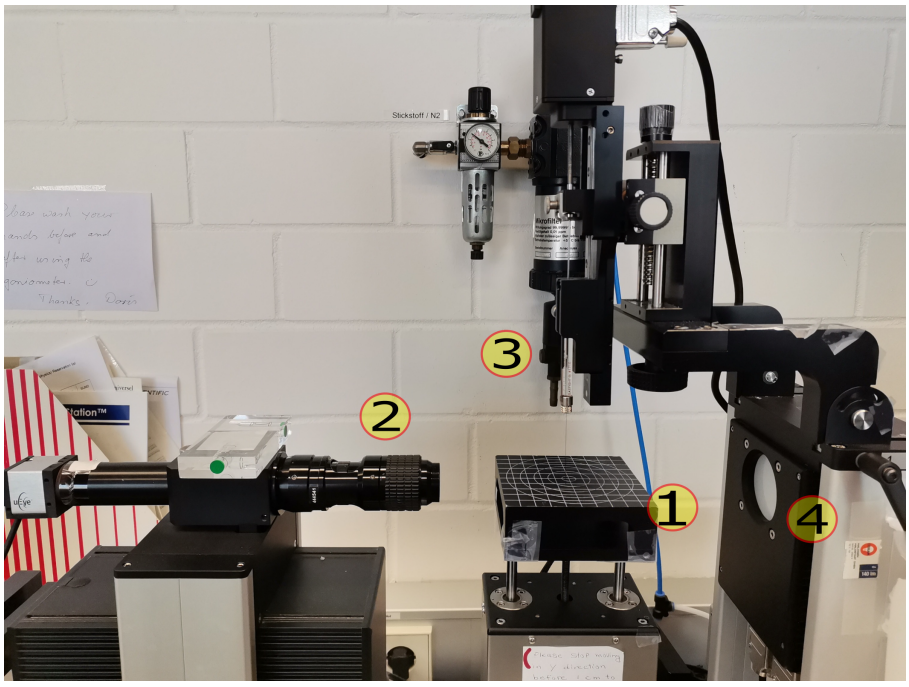

Figure 3.1: Picture of the Goniometer setup, 1) Stage: The stage can move in 3 dimensions and also can rotate to measure roll-off angles. 2) Camera: The camera is equipped with an objective to focus the drop. 3) Syringe. 4) Illumination.

3.2 Droplet Probe

The droplet probe technique requires the attachment of a micro-sized drop to a tipless cantilever (NSC 35-12 MikroMasch of 8.5 N/m and 0.03 of force constant respectively) in order to perform force measurements in the AFM. To attach the droplets we use a micro-manipulator and a optical microscope. First we place a few microliters of liquid on a glass slide and contact with a tipless cantilever. If the cantilever is too hydrophobic, it's useful to use a non-coated cantilever to place smaller drops on the glass slide first. It has also been observed that drops resting on a fluorinated slide attach to the cantilever easily, due to the reduced adhesion exhibited with the coated surface.

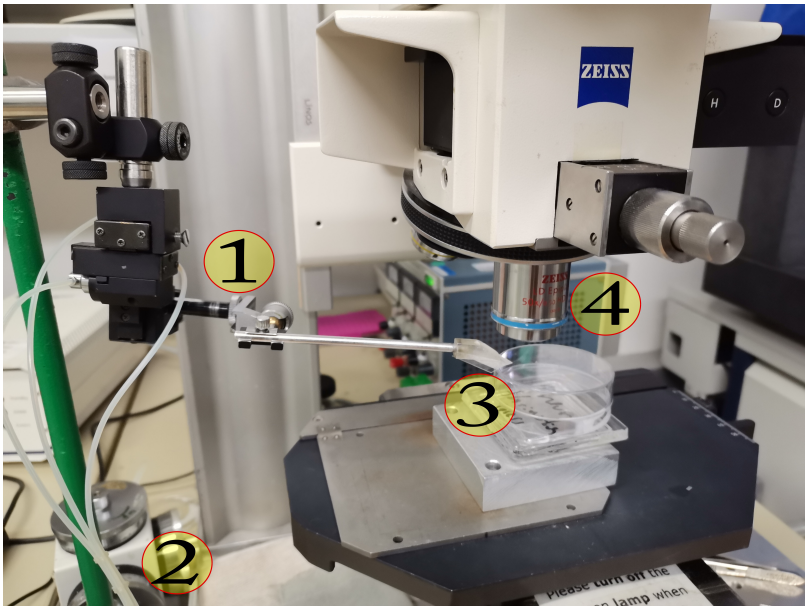

Figure 3.2: Image of the 3-axis oil Micromanipulator. 1) The arm of the micromanipulator is moved by oil from the controller. 2) The micromanipulator controller changes the pressure of the oil provoking the movement o the arm, the control has three knobs for x,y and z movement. 3) On the edge of the arm a glass slide is glued with double-sided adhesive tape, on to which our cantilevers are attached. 4) The microscope has 3 objectives (x5, x10 and x50) depending on the desired magnification.

3.2.1 Cantilever Fluoranization

In order to obtain droplets we need to avoid wetting on the cantilever, to achieve this, it is useful to make the cantilever hydrophobic and obtain a contact angle above $30°$, the time of the fluoranization depends on the droplet and the cantilever composition.

Fluoranization process

As in the case of the soot template surface, for the fluoranization of the cantilevers we use CVD technique.

- Plasma Cleaner: We put the cantilevers in the plasma cleaner for 5 minutes at 100% of capacity.
- Desiccator: We put the cantilevers in the desiccator with $100\mu L$ of trichloroperfluordecylsilane at $50[mbar]$ for 30 minutes.

3.3 AFM Measurements

The AFM force measurements were performed on a JPK IV NanoWizard® SPM, mounted on customized stage that allows the integration with Confocal microscopy. This stage is inspired on the factory stage of JPK, and include all the function of the original stage, this mean movement in both directions of the AFM head, and movement of the sample.

AFM Head

The AFM head have screws to move the laser(Fig.3.3), the PSD and the mirror. These alignment screws allow us to place the laser spot on the cantilever and center its reflection on the PSD detector(figure 3.3).It is necessary to align this 3 components using the screws shown in figure 3.3(2) where we can move the laser beam, the PSD and the mirror independently.

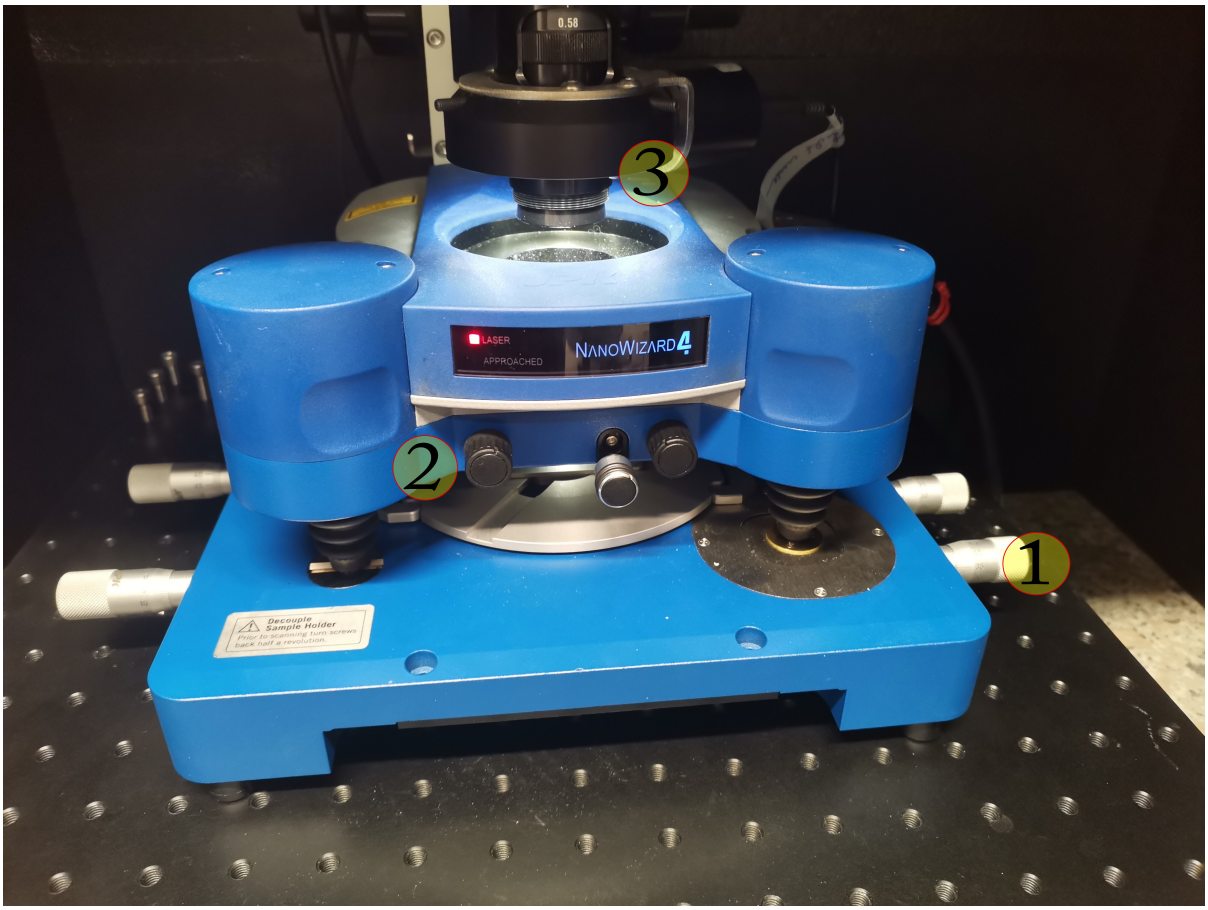

Figure 3.3: AFM head mounted on stage 1) The stage is able to move the AFM head and the sample holder. 2) Screws to align the laser and the PSD. 3) Top view microscope: To facilitate the alignment and to find the desired spot of scanning it is useful to implement optical microscopy. The AFM head and stage are designed to be able to use an optical microscope on top or below the AFM.

3.3.1 Spring Constant and Deflection Sensitivity

The NanoWizard IV software controller allows us to record the deflection sensitivity thermal noise of both vertical and lateral deflection. For vertical deflection, the software itself has the option to fit the thermal noise spectrum and calculate the deflection sensitivity and the cantilever spring constant (figure 3.4).
For the Lateral Deflection, we can record the thermal noise, nevertheless we need to use an external program to fit the curve, this program was provided by JPK.

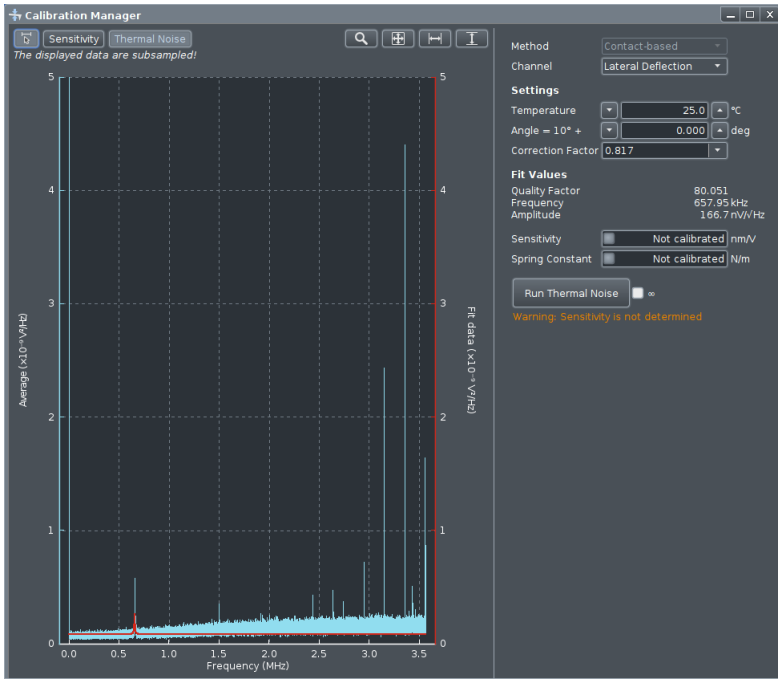

Figure 3.4: The calibration manager module of JPK software provides the option of record thermal noise of the lateral deflection, the peaks correspond of the natural torsional frequency

3.4 LFM

For the lateral force measurement, we need to calibrate the cantilever first, for which we select contact mode. The AFM records all the signals as usual, but this time the lateral deflection is shown in Newtons. One of the most important procedures is to set the I-Gain and P-Gain, since the drop is more sensible than a tip to vibrations, this step is crucial to obtain reliable LFM data and confocal images. Given that it as is not possible to set the lateral deflection on the center of the PSD, we can not trust the trace and retrace as the real friction value. This is why we need to create a new channel that shows the difference between the trace and retrace channel, showing the actual value of the friction on the surface. To achieve this, different programs can be used to process the data from the AFM, in this case the AFM data was exported as a 3D map and Python was used to visualize the profiles and process the data. In general, for LFM we can extract the offset:

$$Friction = \frac{Trace - Retrace}{2} \tag{3.1}$$

Where Trace and Retrace channels are a matrix, we can create a new matrix with the new values, and we can see the map of the accurate forces on the surface, nevertheless the Trace and Retrace are useful for qualitative analysis.

3.5 Confocal Microscopy

Commercial LSCM are very precise and reliable equipments, nevertheless the setup is too compact and is not easy to customize and combine with other experiments such as AFM. This is why we implement a home-built LSCM with the purpose of integrating it to a commercial AFM system (Fig.3.5). In this section we will discuss the basic characteristics and functioning of this microscope. From Fig. 3.5 we

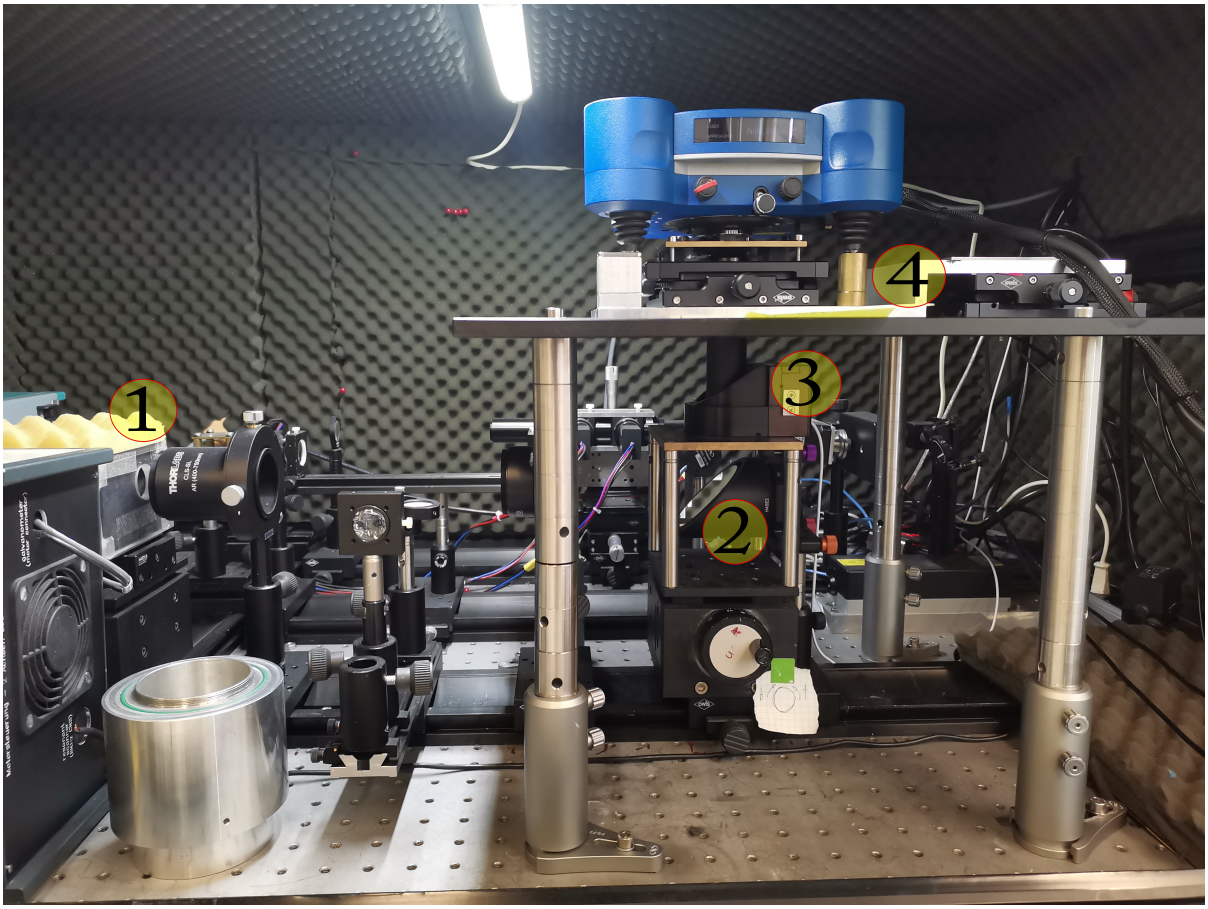

Figure 3.5: Setup of LSCM-AFM experiment 1) Source of the laser beam. 2) Mirror: this mirror direct the source light to the objective, the mirror doesn't correspond to a beam splitter. 3)Objective, the objective is mounted on a piezo stage that allow it to move in 3 dimensions to scan the samples, in this case the objective used is an Olympus 40x/0.95na 4) AFM stage, the AFM stage with the AFM head on top.

can see the main parts of the confocal.

3.5.1 Setting and use

The LSCM work with 2 diode-pumped solid-state lasers of 473nm (Cobolt Blue) and 532nm (Cobolt Samba) wavelength and an output power of 25mW. The light is received using 3 detectors, the reflection channel and 2 channels for the light emitted by fluorescence. The LSCM controller runs with LabView®, which allows to control different signals of the Microscope. We are able to select each channel and also see the 3 channels at the same time. The objective used is an Olympus 40x/0.95na

XY and XZ planes

The confocal microscope allows us to measure in 2 different planes, while XZ gives us a profile of the drop surface interaction, XY is useful to see the contact line area of the liquid-surface interaction,

beside this, XY plane is used to make 3d structures.

3.5.2 Confocal Calibration

Although the microscope software records the images with the pixels scaled, the refractive index of the coating can affect the dimensions of the imaging, so it is useful to use micropillar arrays to check the correlation between the pixels and the real distance or improve it if necessary. Given that the shape of the pillar is well known, a simple profile is enough to measure their height and the diameter. To have the real dimensions of the pillars AFM imaging is used, when we compare the profile extracted from the AFM map (Fig.3.6 b)) with the dimensions of the confocal, we can observe a match in the pillar height and width.

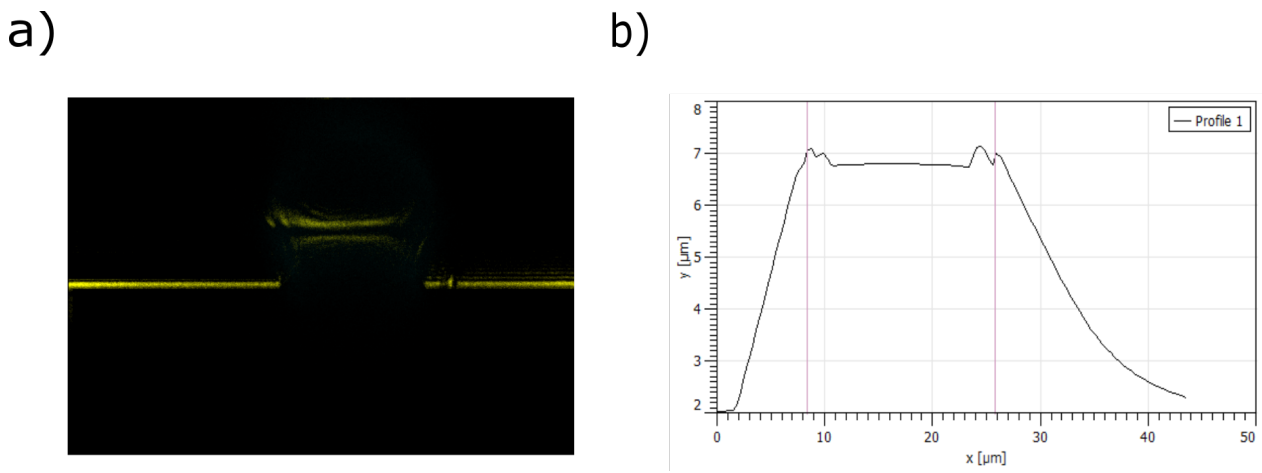

Figure 3.6: a)LSCM of pillar arrays, the confocal is configured to save the image as .tiff files including the pixel-μm scale. b) Profile of the AFM measurement of a pillar.

3.5.3 Liquid and Dyeing

In general, the study of wetting is made with water, nevertheless the vapour pressure on micro-sized drops provoke a fast evaporation, for water this is almost instant. This is why we need to find liquids with different composition that evaporate slowly.

Water-Glycerol

A known way to avoid evaporation of drops is to mix water with glycerol[19], the ideal composition is (40%) of glycerol in the solution, which yields a ST of $70[mN/m]$. Nevertheless, when we dyed the solution, the ST decreases dramatically, to avoid this we reduce the glycol from 40% to 15% and then we obtain a ST of $67[mN/m]$, witch is high enough to good superhydrophobic surfaces (regular superhydrophobic surfaces did not work for liquids under $67[mN/m]$). For dying the water-glycerol solution Atto 532($1.4\mu M$) was used. Atto 532 is a hydrophilic dye that is widely used for LSCM. After dissolving the dye in the water-glycerol solution the final ST is $67.51 \pm 0.49[mN/m]$ (using a tensiometer, the result of the measurement is shown in figure 3.7b).

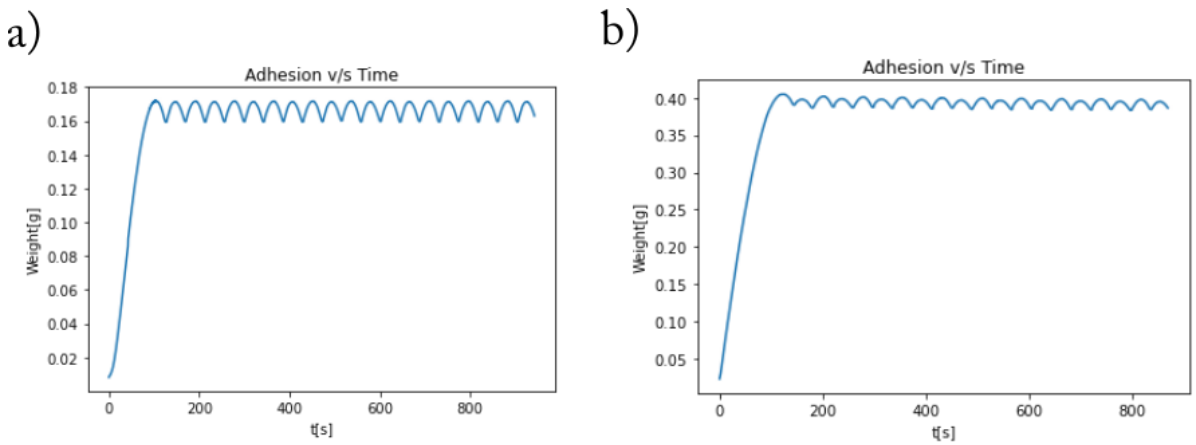

Figure 3.7: a) The graph show the ST measuring for dyed ionic liquid (see section 2.3), the average of the (local) maximum weight is 0.17193 g. b) Graph of the water glycerol mix, the average of the weight is 0.399 g.

Ionic Liquid

We also used ionic liquid, given their low vapour pressure. in particular *Trihexyltetradecylphosphonium bis(trifluoromethylsulfonyl)imide* has been used. Ionic liquid are salts in liquid state. Ionic liquids have a very low surface tension (around 30[J/m]), so we can use it to test oleophobicity. The main reason to use ionic liquid is its stability, the low evaporation allows long time measurement without material loss.
To dye our ionic liquid we use Rodamine 6g, which is hydrophobic and has to be mixed with an alcohol first. Once the dye is mixed homogeneously with the alcohol we can mix it with the ionic liquid, the ST measured is $25.75 \pm 0.03[mN/m]$ (figure 3.7 a).

AFM orientation

Depending on the information we want to obtain for the measurement we can use different orientations of the AFM on the Setup, For the normal force measurement is convenient to observe the profile of the cantilever. On the other hand, for the friction measurements, it is necessary to see the the cantilever from the front and thus we can observe the contact angle hysteresis as the cantilever maps the surface.

Sticky Point

Sticky Point is a very useful procedure to attach liquid droplet to the end of a tipless cantilever, this procedure consist of using a FIB to make a hydrophilic spot on the fluorinated cantilevers, basically we are removing the hydrophobic coating, to avoid the drop from sliding through the cantilever and also we can control the size and position of the drop itself. Figure 3.8 show a SEM image of the cantilever after FIB treatment.
With a sticky point, it is easier to attach droplets to the cantilever.

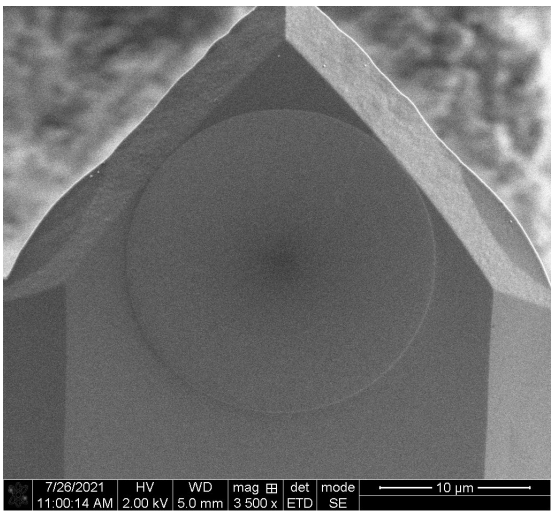

Figure 3.8: SEM image of the sticky point.

Chapter 4

Results and Analysis

4.1 Surface Characterization

4.1.1 SEM and AFM

SEM imaging was used to observe the quality of the surfaces, giving information about the main characteristic of the two surface. AFM imaging also gives us precise information about the topography of our surfaces.

Soot Template

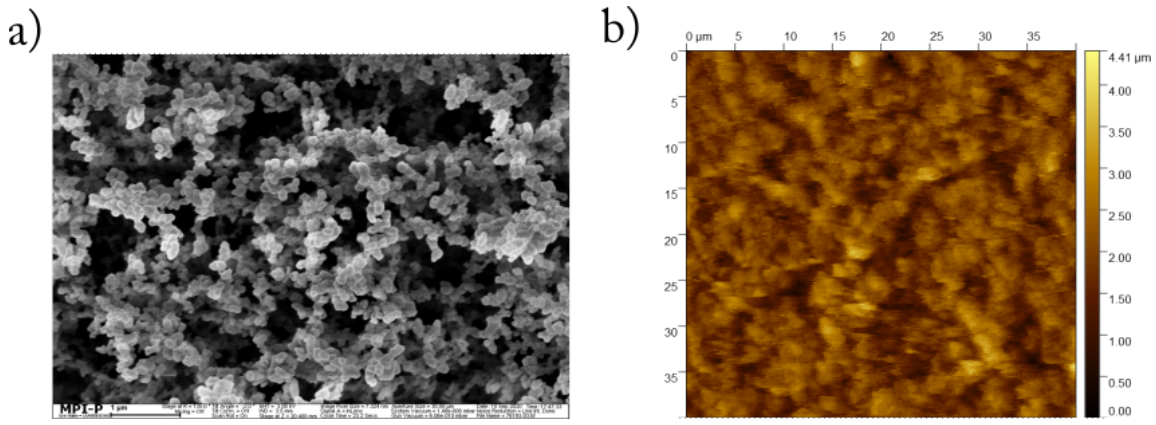

Figure 4.1: a) SEM image of soot template surface $7.5 \times 5.5 \mu m$. b) $40 \times 40 \mu m$ AFM map of soot template surface.

From the SEM image we can see the quality of the Silica Shell, the shape is consistent with the soot structures, where each soot structure has a width between 100 and 200 nm. This structures have very small contact with the liquid, then a Cassie Baxter state would explain the high repellance with water.

Nanofilaments

Just as in the case of the soot template surface, the structure formed by the silicon filaments allow the surface to be superhydrophobic (Cassie-Baxter state), nevertheless the nature of the nanofilaments is very different from the silica shell, the nanofilaments are grown by a chemical process, then the size and shape depend on different parameters, the SEM image show nanofilaments of $70nm$ of width.

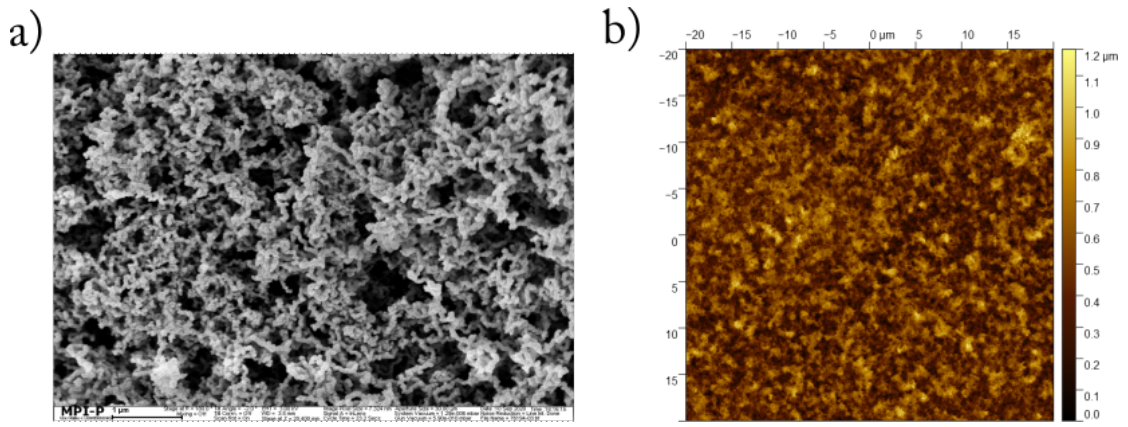

Figure 4.2: a) SEM image of nanofilaments surface $7.5 \times 5.5\ \mu m$. b) $40 \times 40\ \mu m$ AFM map of nanofilaments surface.

4.1.2 Contact Angle

The CA for both surfaces was measured using a goniometer, the static contact angle was measured with Ionic liquid in the case of soot template and Water-Glycerol mix for the nanofilaments. Ionic liquid on soot template show a contact Angle of 160° with the surface(figure 4.3). The main reason to use one liquid to each surface is that it was not possible to obtain oleophobic nanofilaments.

Soot Template

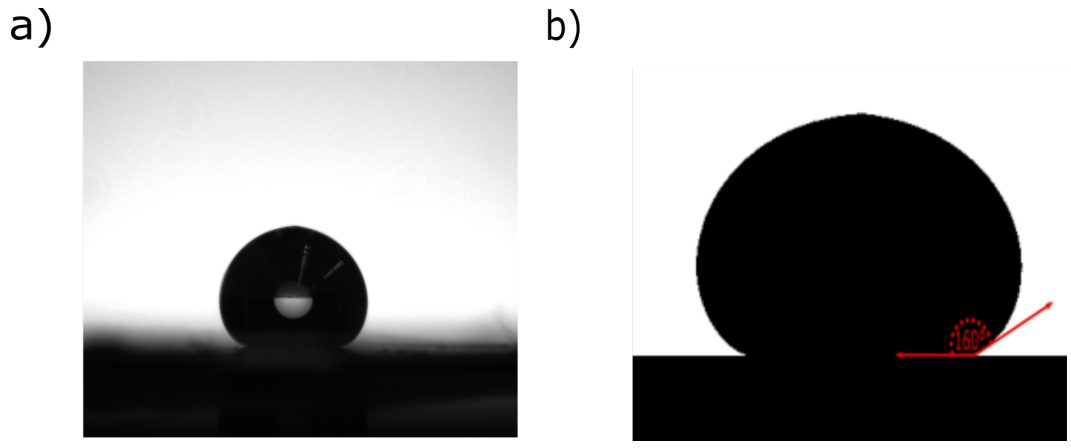

Figure 4.3: a) Picture of the drop taken from the goniometer. b) Binarization of the picture with the contact angle measured.

Nanofilaments

The CA measured on nanofilaments is 161° for water glycerol mix(figure 4.4).

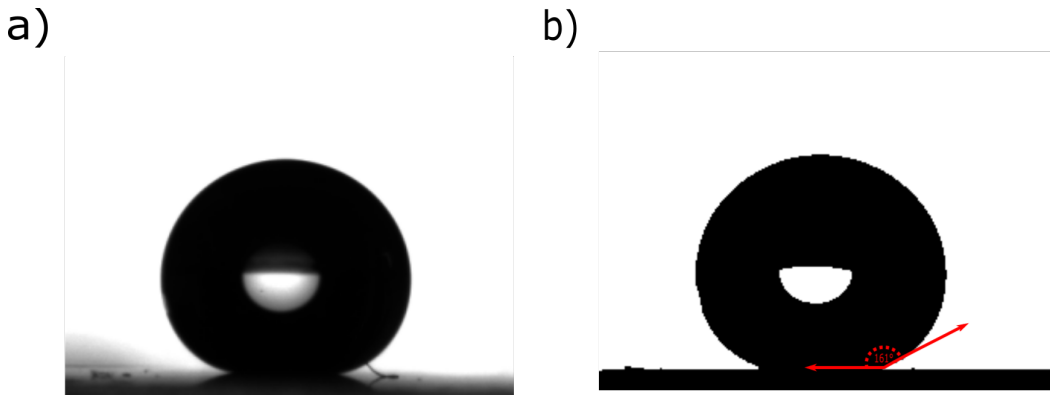

Figure 4.4: a) Picture of the drop taken from the goniometer. b) Binarization of the picture with the contact angle measured.

4.2 Adhesion Force

Before performing AFM-Confocal measurement is important to analyse the force curves of the liquids interacting with the surfaces, by looking at these curves we can measure the(ionic liquid on soot template unless otherwise indicated) maxim adhesion the snap in and pull out forces. In the Fig.4.5 we can see a force curve of a ionic liquid drop on soot template. In this measurement, the maximum force is 34.7 nN (green dashed line), that correspond to the setpoint force. The maximum adhesion(min force, orange dashed line) is 703.18, the snap is -259 nN (red dashed line). The area under the curve, defined as the work of adhesion is 3.7 pJ, which corresponds to the work necessary to detach the drop.

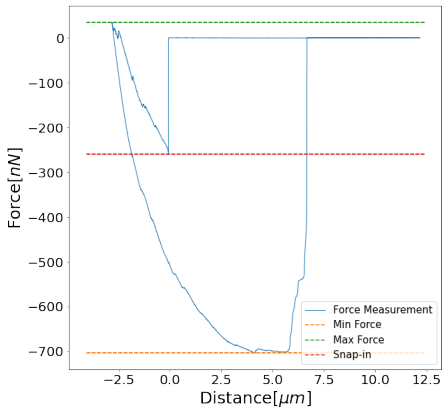

Figure 4.5: Force curve of a ionic liquid drop on soot template

Adhesion in Time

To test the quality of the surface, a useful procedure is to check the change in the adhesion (minimum force) of the drop in the surface after many approaches, in Fig.4.6 the adhesion vs the number of the force test for soot and ionic liquid is showed. For all the normal adhesion force measurements, the 8.9 N/m cantilever was used. If we compare this set of force measurements with the force curve showed before we can see that there is a big difference in the adhesion value, this can be due to different contact

area between the drop and the surface or due to surface defects, nevertheless we can't know without visualizing the drop interaction.
After 80 approaches, the adhesion decreases around of 1 nN, this change is a 0.37% of the initial force adhesion. The reasons for this diminution of the force can be due to evaporation. Another reason could be the charging of the surface and the drop, affecting the sensitivity of the cantilever.

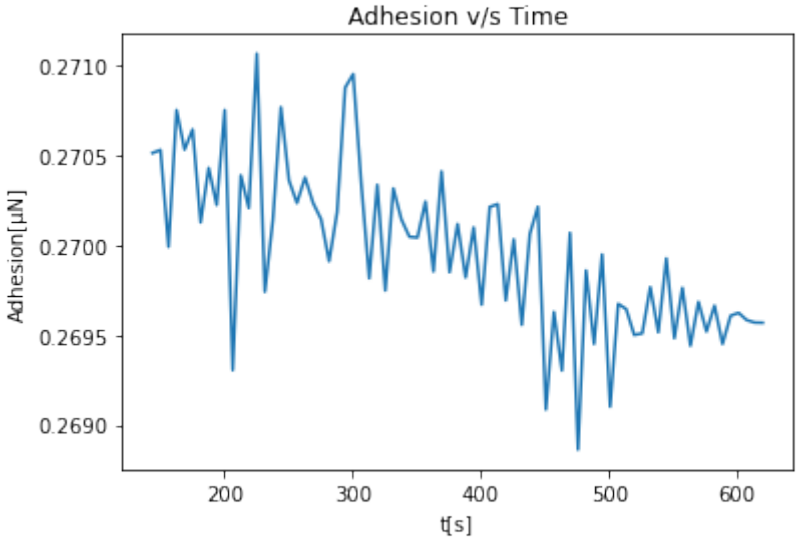

Figure 4.6: Adhesion in time

If we consider the change in the adhesion, we can say that the force curve remain constant in time and the quality of the surface is conserved. This means that a single force curve is representative of the behaviour of the drop.

4.2.1 Adhesion Measurement Imaging

We start using confocal microscopy to measure static droplets mounted on cantilevers. LSCM has the advantage of taking 3d samples, allowing us to measure the drop volume and surface. For a pinned drop, it is also possible to measure the contact line and contact area.

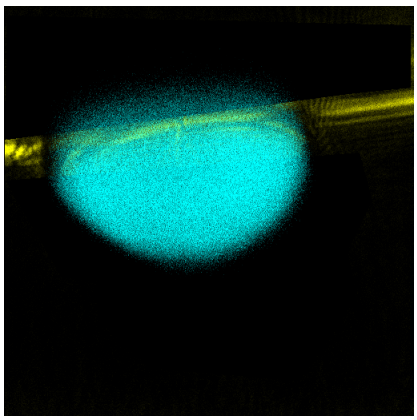

Figure 4.7: Confocal image of cantilever with drop attached, the contact angle between the drop and the cantilever is 90°.

As we see in Fig.4.7, from the confocal image, we can extract important data of the drop attached to the cantilever, the height of the drop $9.5\mu m$ and its diameter 18 μm are used to calculate the volume, in this case 1.65 pL, assuming the drop as a semi-spherical shape, also we can extract the contact angle between the drop and the cantilever(90° from the figure 4.7).

4.2.2 Low Quality Surfaces

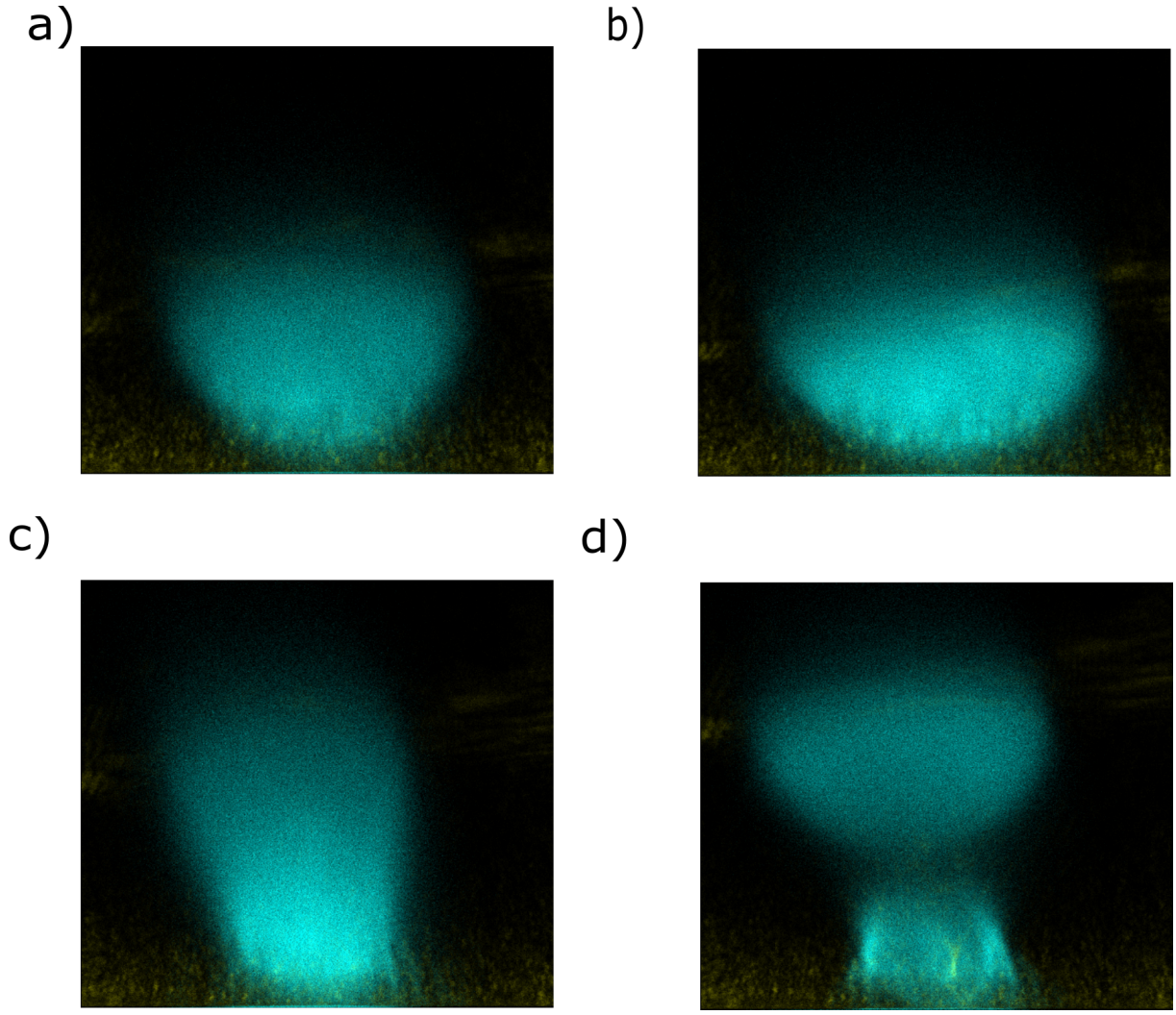

Figure 4.8: Sequence of the XZ plane measurement video. a) The first frame of the video showing the droplet interacting with the surface. b) The cantilever starts retracting from the surface provoking a change in the contact line. e) The frame showing the moment just before the drop loses its contact with the surface(pull-out moment). d) The cantilever is fully retracted and we can observe a remnant drop on the surface.

Part of the work of this thesis, is to find good quality surfaces, i.e, that are both superhydrophobic and transparent. an example of a poor quality surface is shown in figure 4.8. This figure shows a water glycerol mixture interacting with a nanofilament surface. Although the surface transparent enough, the remnant drop on the surface is considerably large, indicating that there is no superhydrophobic behaviour at microscopic level.
This qualitative result is important to test the repellency of the surface, because even when we have a high macroscopic contact angle (150° for this particular surface), we don´t have high repellance with the surface and this mean that the surface wets.

4.2.3 How Does Confocal Imaging Affect the Force Measurement?

LSCM uses an objective coupled to a piezo-stage witch scans the laser over samples. This piezo-movement can cause vibration and affect the measurement. It is necessary to test how this vibration can affect the measurements.

To check this influence, we use an superamphiphobic soot template surface and make a force measurement without scanning the confocal laser. Once this curve is recorded the LSCM is turned on with different magnifications and the force measurement is repeated for each. When the lowest magnification is used, the force curve is affected considerably Fig.4.9 b), this is because the piezo moves with a bigger amplitude in order to scan the sample. As we increase the magnification, this amplitude is reduced and thus, the vibration over the cantilever and the surface is considerably less, and practically negligible as showed in Fig.4.9 d).

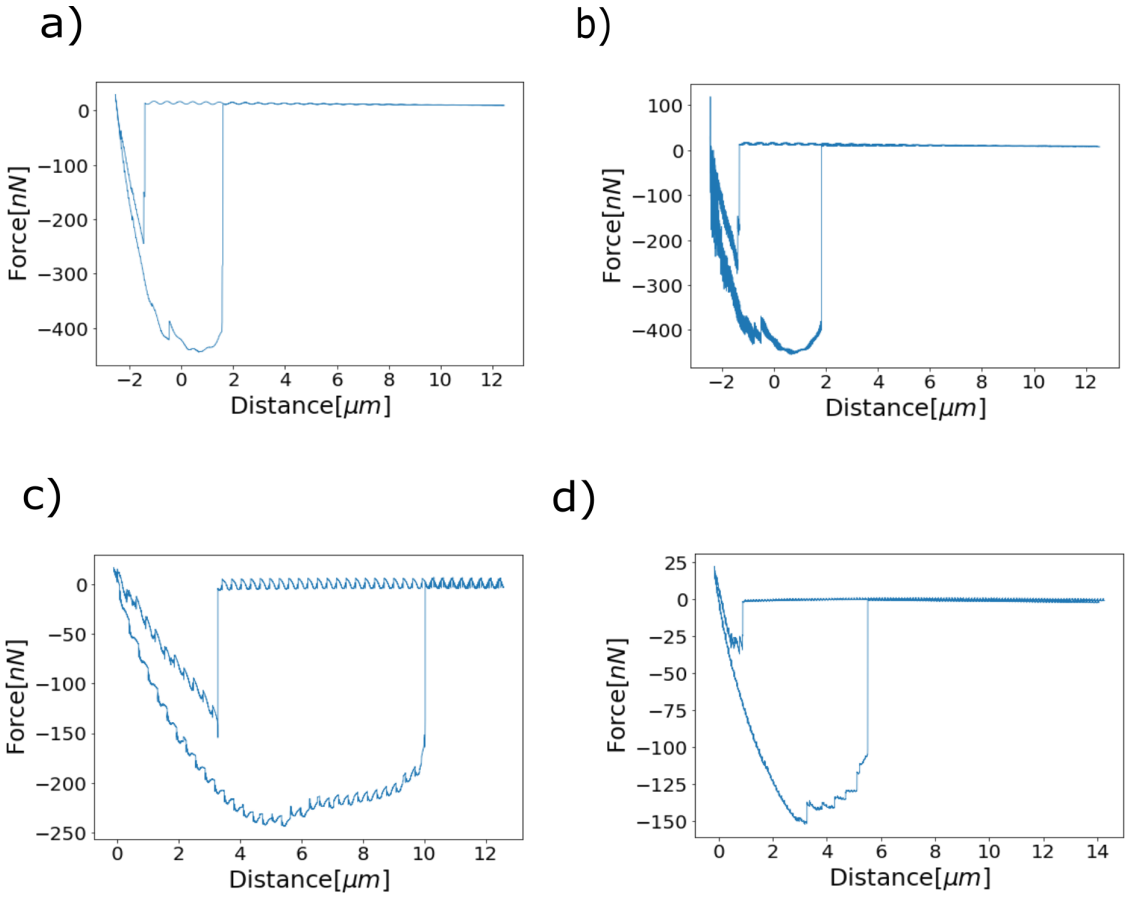

Figure 4.9: Force curve measurement for different scan sizes, using ionic liquid on soot template. The graphs a) and b) correspond to the same measurement before and after turning on the LSCM. The graphs c) and d) correspond to different experiments but the same surface and liquid.

4.2.4 XZ Measurement

The first approach to make AFM force spectroscopy with LSCM is to take a XZ plane video of the force measurement and see the profile of the drop-surface interaction. The main challenge of this measurement is to have a good resolution to appreciate the contact angle while the force measurement is running. To have the best resolution possible, an average of 32 frames was used. Each frame takes 5 seconds, so it is not convenient to record continuous force curves, i.e, a trapezoid or a triangle like curves as a function of time. Instead, we can make custom height-time and force-time functions. For this purpose a step by step function was designed. Given that the snap in moment is practically instantaneous, we start the video capture after the snap in. The approach was continuous with a speed of 100 nm/s and a setpoint of 5 nN. After the snap-in the cantilever starts retracting with steps of 0.1 μm at a speed of 100 nm/s every 7 seconds (figure 4.11b). After 24 steps(the maximum possible by the software), the cantilever retract continuously at 100 nm/s.

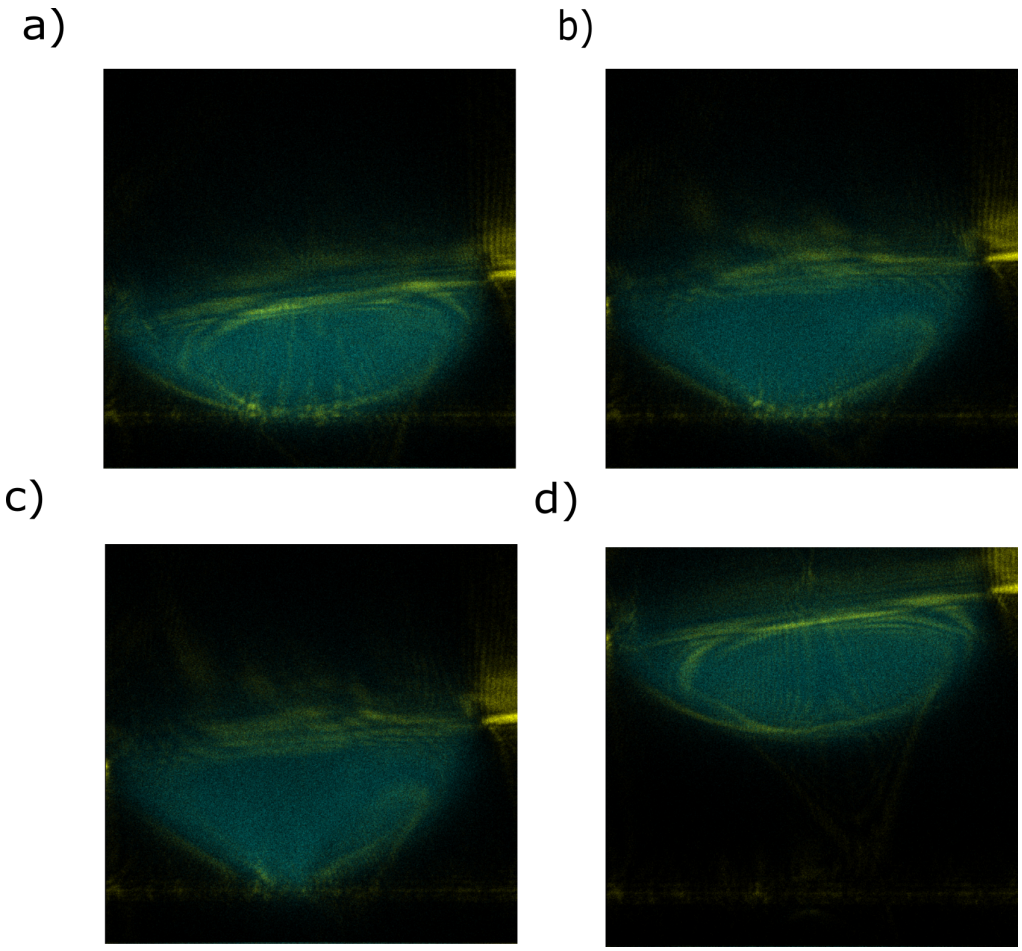

Figure 4.10: Sequence of the XZ plane measurement video, a) The first moment of the video, we start recording after the drop land on the surface with a setpoint of 50 nN, then after 10 s the tip start retracting. b) The tip have change the height provoking a change in the contact angle. e)The step before the pull out moment, this is the last moment before the drop completely lost contact with the surface.d) The drop is away from the surface and doesn't feel more relevant forces and returning to its original shape.

From the force-time and height-time graph we can see that the force is not constant in each step, this could be to the relaxation of the contact line, nevertheless this does not affect the main components a force curve, i.e, still having a maxim force, snap-in and pullout moments.
For the video, we zoom until the drop size is reached in order to have the best quality possible and to avoid noise. In Fig. 4.10 we show a few steps of the video itself, we can observe the moment after snap-in, the first instances after the cantilever starts retracting, the moment before the pull-out moment and the drop retracted.

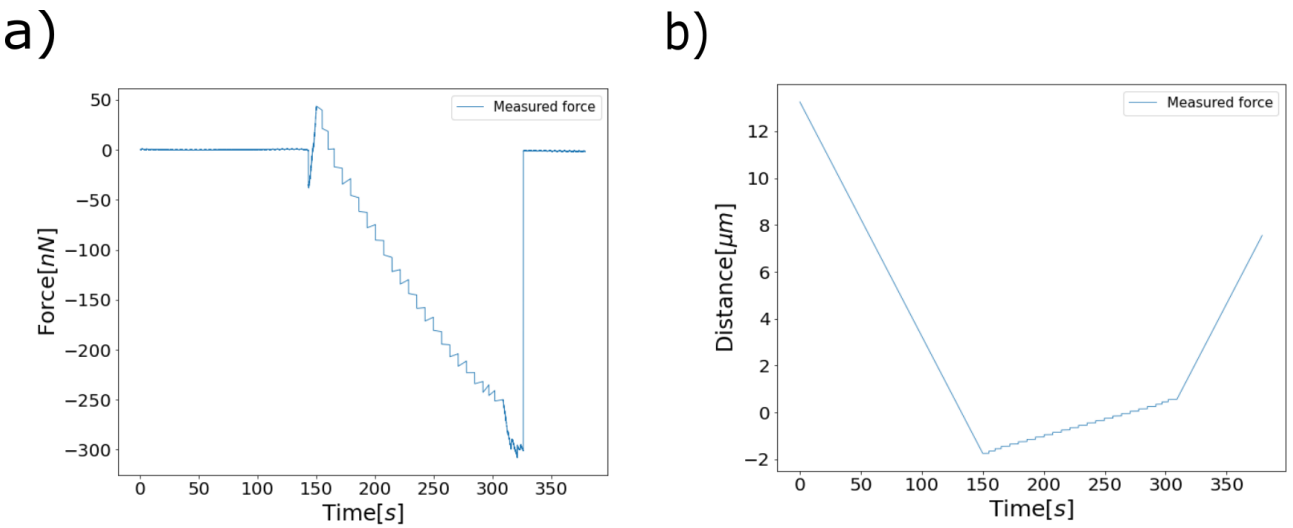

Figure 4.11: a) The graph shows the force in time, we can see that in each step the force is not constant, this is because the AFM channel is configured to keep a constant height. b) Height v/s time graph, we can see that the steps are very well define.

Force Measurement Result

In figure 4.12 the force curve of the XZ measurement is shown. As we can see the force curve itself is not severely affected by the relaxation of the contact line, and we can extract the main information of the experiment. The adhesion is $307.8nN$ and the pull out is $300nN$, this values are very close, a possible reason is the time that the drop was in contact with the surface. The work done by the cantilever to detach the drop is $0.78pJ$.

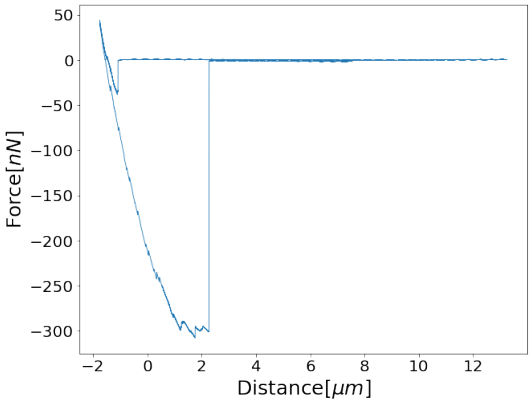

Figure 4.12: Force measurement of the drop interaction, the curve itself is not affected by the step by step function.

4.2.5 Contact Angle

Using image processing we can track the drop shape and extract the edge of the drop, by fitting this shape we can extract the contact angle between the surface and the drop (figure 4.13).

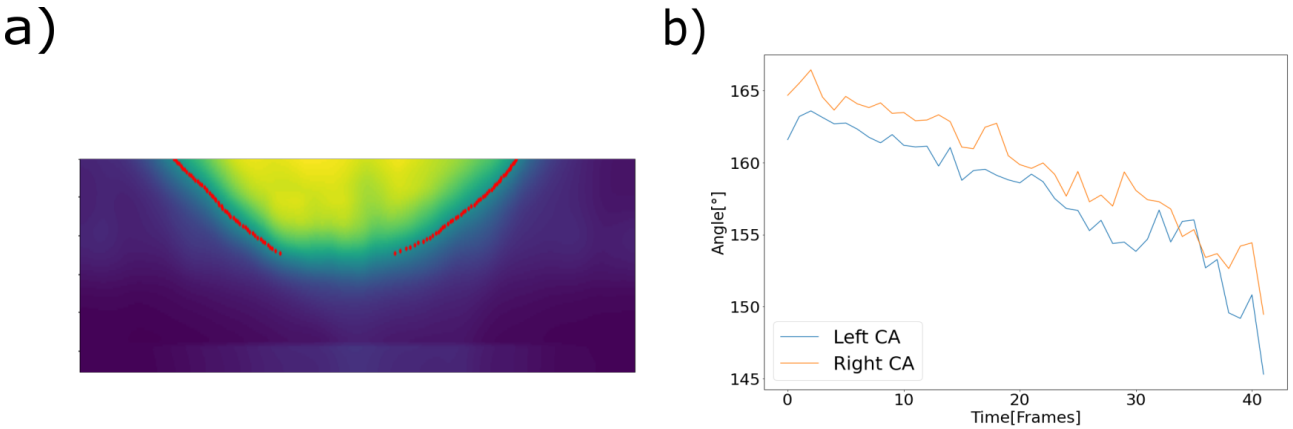

Figure 4.13: Sequence of the XZ plane measurement video. a) Edge detection of the drop. b) Result of the angle decreasing in time(extracted from the video)

Analysis

If we consider a symmetric drop, we can use the profile to obtain the contact area with the contact radius r (figure 4.14 a), and the curvature of the drop using the initial drop shape gives us the Laplace Pressure P_0=2710.52 Pa from equation 1.4. With these values and the contact angle we can calculate the adhesion force using equation 2.28 and compare the results with the values obtained by AFM force spectroscopy. As we can see in figure 4.14 b, the values of the calculated force follow a similar behaviour as the measured Force, but it does not reproduce the measured value of adhesion correctly.

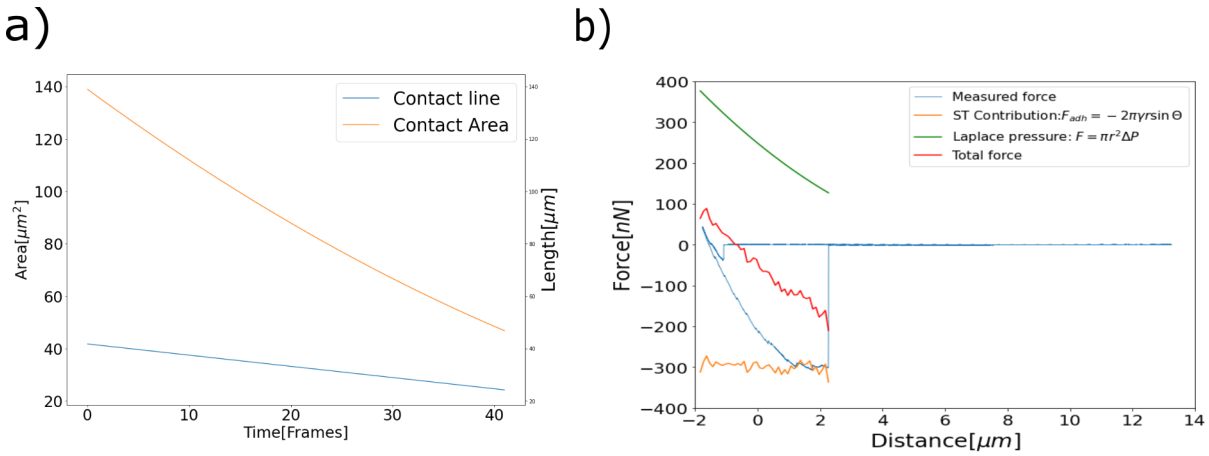

Figure 4.14: a) For the calculation of the contact line and the area, we assume that the radius decreases linearly, then we use the initial and final value of the contact line radius, this assumption will be justified with the 3d experiment imaging. b) Comparison between the forces calculated from the video and the actual measured force.

Calculating the Laplace pressure

As we can see in the figure 4.14, the Laplace pressure gives us a logic value for the first moments of the measurement, nevertheless as we retract this value is not accurate since there is a change of the drop shape. To fix this we can solve a simple equation to obtain the correct result.

$$F_{st} - \pi r^2 \Delta P = F_{measured} \tag{4.1}$$

As we obtain the new values of the Laplace Pressure we can see from Fig.4.15 a) the values obtained, is interesting to see that the initial value for the Laplace pressure is $2500Pa$ which is very close to the calculated value, the main reason for the difference is that we are using a symmetric drop assumption.

a)

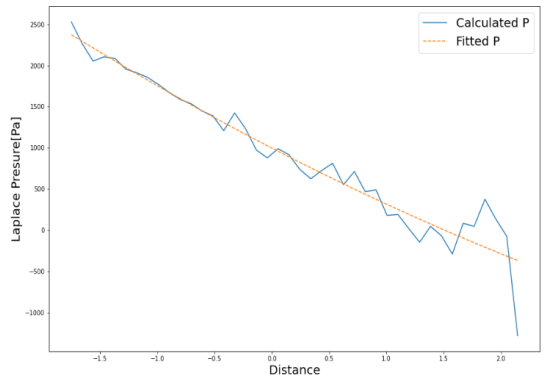

b)

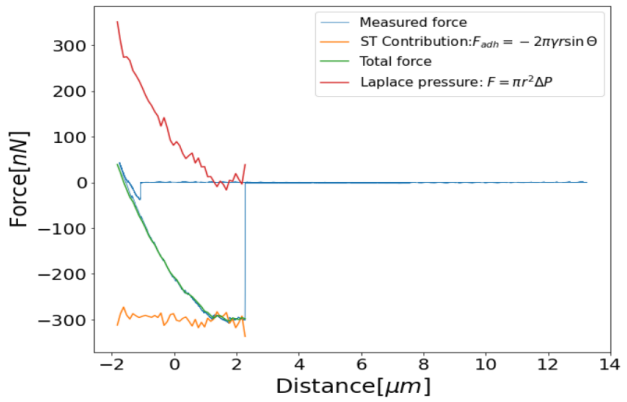

Figure 4.15: a) Calculated value of the Laplace Pressure, we can fit this calculated curve obtaining a relation between the Laplace pressure and the distance: $38.64x^2 - 719.16x + 997.7$. b) As we use the equation 4.1 to obtain the Laplace pressure, the calculated capillary force and the measured force are equal.

Pros and Cons

The principal advantage of this method is the good quality of the force curve, as each step is around 7 s, the time step is short enough to avoid the drop from interacting in any other way (as we will see in the next experiment). Also with this procedure we obtain a good quality images , that allow us to measure contact angle. The principal disadvantage is that we can not have the exact contact angle because the LSCM is not precise enough to locate the XZ plane in the center of mass of the drop, so we are not taking the exact profile as with an optical camera.

4.2.6 3D Measurement

We use the procedures described in the previous section and implement the step by step method to make a three dimensional video of the drop interaction. As the 3D Videos take 110 second for frame, we follow the same procedure used for the XZ plane video, but this time each step takes 110 s. The obtained results give us important information, such as the pinning area, the contact angle and the surface of the liquid-air interface. With the liquid-air interface we can obtain the curvature of the drop and thus the Laplace pressure.

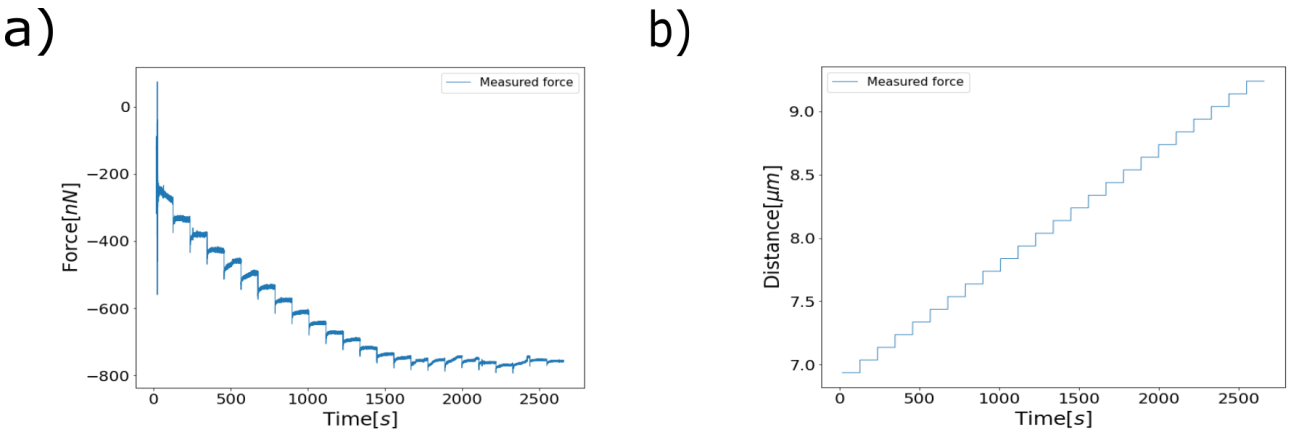

Figure 4.16: a) The graph shows the force in time, we can see that in each step the force is not constant, this is because the AFM channel is configured to keep a constant height. b) Height v/s time graph, we can see that the steps are very well define.

Pinning Area

The 3D structures made by the LSCM software are built from 2D images that we stack to get the 3D information. With Fiji software we can extract the XZ profile of the sample and select the plane where the contact line is located, thus, by selecting this plane it is straightforward to measure the area. The pinning area is useful to calculate the contribution of the Laplace pressure on the force, but also, if we consider the work calculated from the force curve we can obtain the work of adhesion per cross-sectional area $w = W/A$. From the graph shown in Fig.4.17 we can see that there is a quadratic relation between time and the decreasing of the Area as we retract the cantilever, here each step represent 110 s but we can easily convert this to distance where every frame is equal to 0.1 μm.

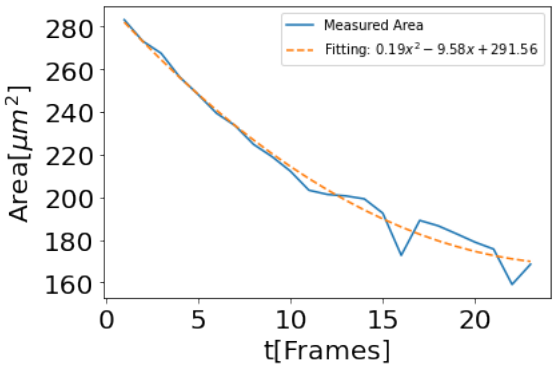

Figure 4.17: Area versus time(frames), each frame takes 110 seconds.

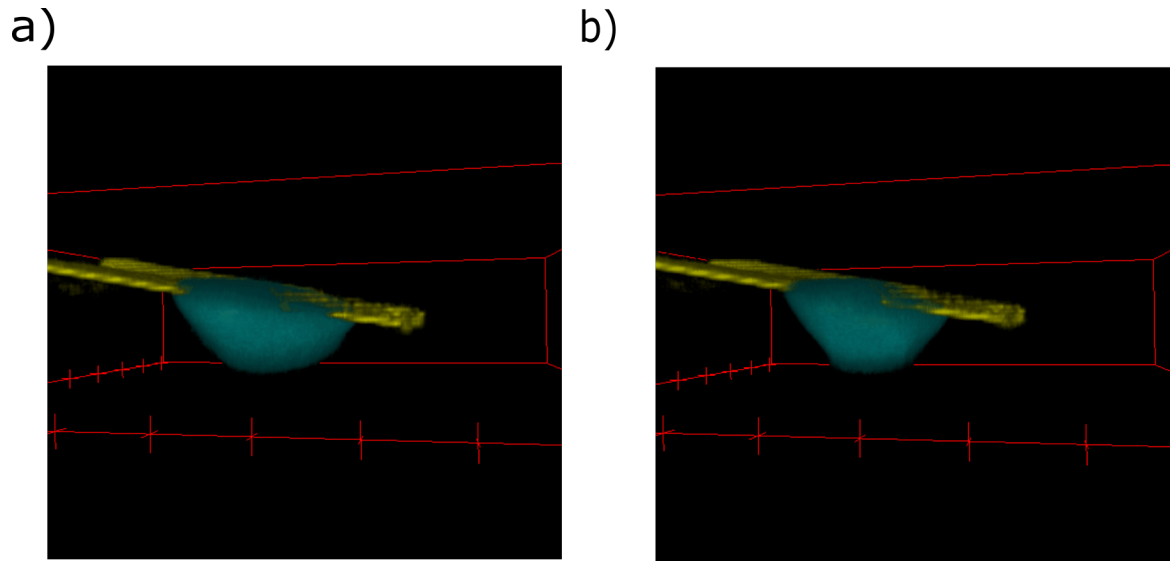

Figure 4.18: 3D video sequence

This procedure allow us to make a 3D video, as shown in figure 4.18, by using this 3d information we can record the drop movement from different orientation and have a more detailed analysis, nevertheless this requires more accurate modeling and fitting.

Force Curve

The pause after each step makes the contact line relax and then the force change, due to this we can not make a correct analysis, but we still been able to obtain information, such as the pinning area.

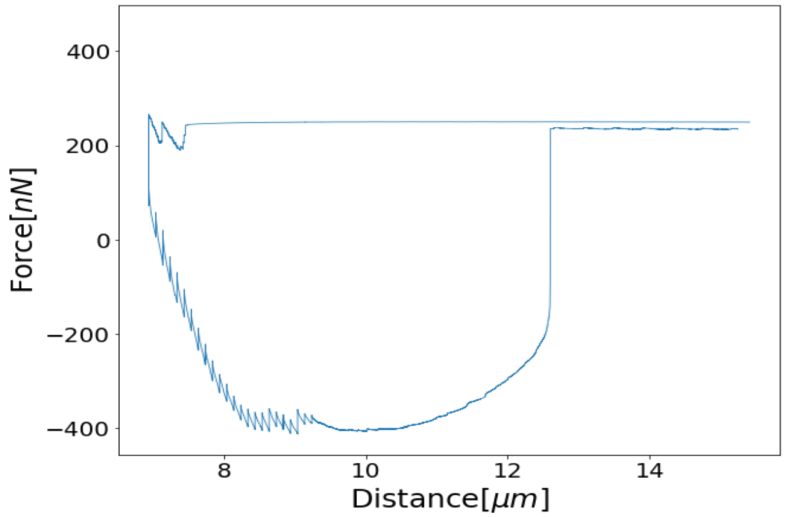

Figure 4.19: Force curve of the measurement, due to the long steps for imaging, there are many displacements in the force on each step, nevertheless the minimum force is not affected and the behaviour of the force on distance is as expected

Discussion

As mentioned above, the 3D method has several advantages such as getting the pinning area, the surface curvature and the contact angle measured at the contact line. Nevertheless, the force-time curve shows that there is a relaxation after each step, making difficult to fit the curve or trust the 3D video, this could be a relaxation of the contact line.

4.3 Lateral Force

As we know, LFM follows the same principle as contact mode AFM, but we also record the lateral deflection. For all the lateral force measurement, the 0.3 N/m cantilever was used. In a friction force measurement with tips we usually have a constant force, given that we need a distance comparable to the tip size to overcome the static force regime.
Nevertheless, given that the size of the drop used as the probe is half of the mapping size, an important part of the forces obtained are from the static regimen of the drop, i.e., when the cantilever is moving but the droplet remains pinned to the surface. Once a threshold force is reached, the drop start sliding and we change to the dynamic regime.

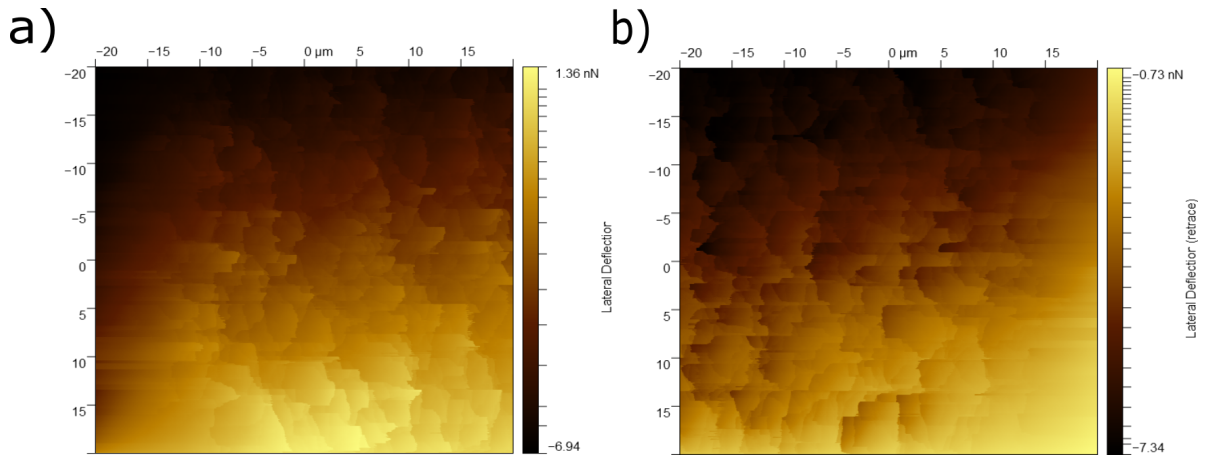

Figure 4.20: a) Trace map of the lateral deflection, we can see the static regime and the friction regime. b) Retrace map of the lateral deflection, the mainly force is negative, since is in the opposite direction of the trace.

In each line we have important information of the friction experiment, this is why making a profile extraction of the data is useful to obtain the force values in the different regimes. Due to the shift of the PSD, we need to define a valid offset to obtain the force values. In Fig.4.21 we can see the profile and the corrected profile plot, where the average of the dynamic regimen friction forces were used to correct the offset.

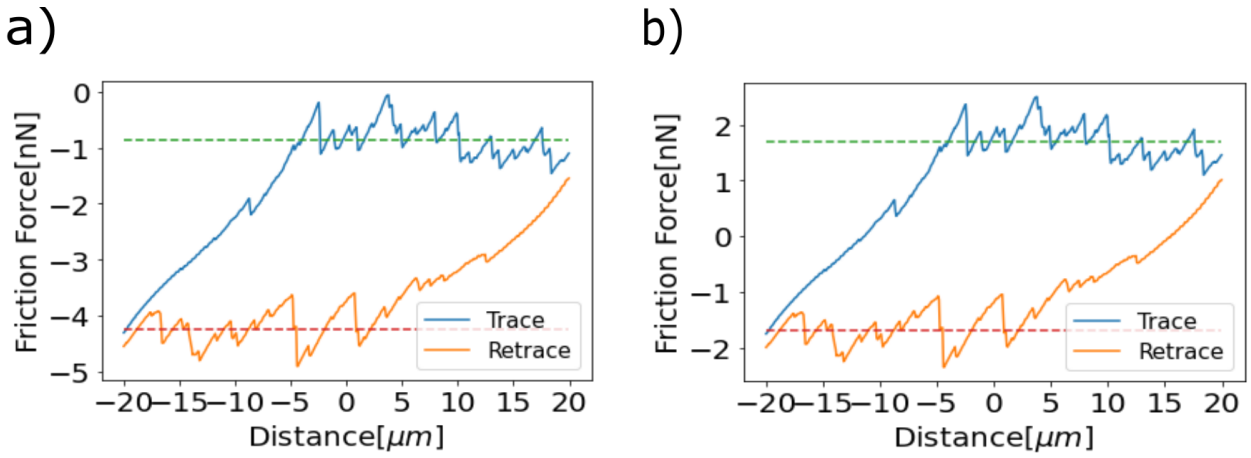

Figure 4.21: a) Trace and retrace profile of the lateral deflection, the lateral deflection values are shifted, we use the average value of the dynamic regime friction to calculate the offset. b) Corrected values, the offset shift to zero and we can make a better analysis of the friction force values.

Force Evolution

The friction force average on each line that map the surface is extracted using equation 3.1, we can plot the friction force on each line and see how it evolves. From Fig.4.20 we can appreciate that the force is not constant and probably there is a diminution, from the graph in Fig.4.22 we can appreciate the numerical values to visualise this force evolution. The curve describes the average force on each line, where every line takes 10 seconds.

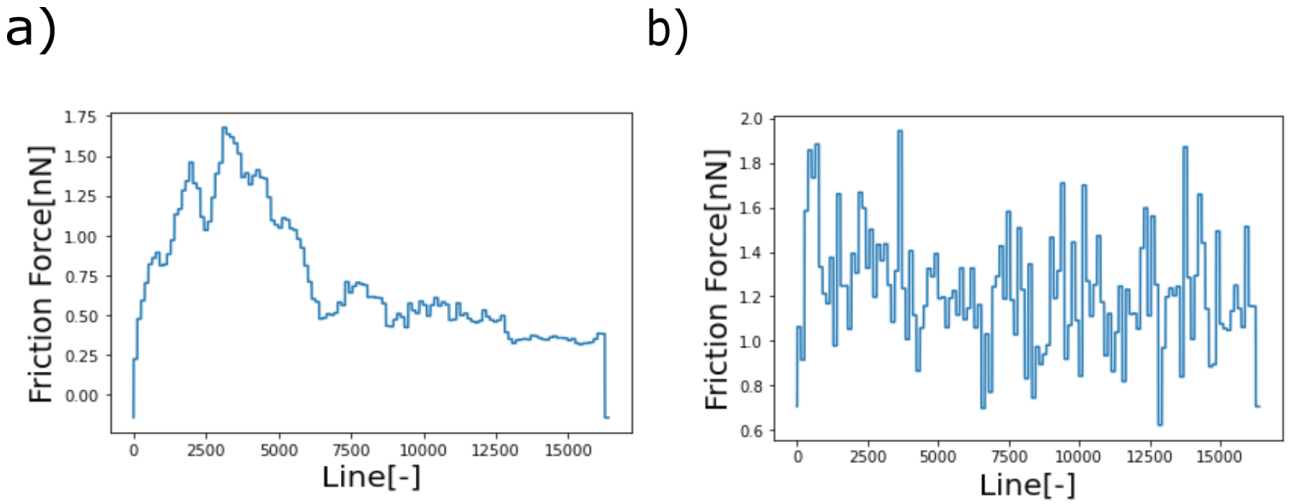

Figure 4.22: a) Friction force evolution for water glycerol mix on nanofilaments. b) Friction force evolution for water glycerol mix on soot template.

4.3.1 Lateral Force Measurement Imaging

LFM results and LSCM are shown in this section. For this experiment we use nanofilaments and the Water-Glycerol mix. First the LSCM images are shown in figure 2.23, and then, in figure 2.24 we show the AFM later force measurements.

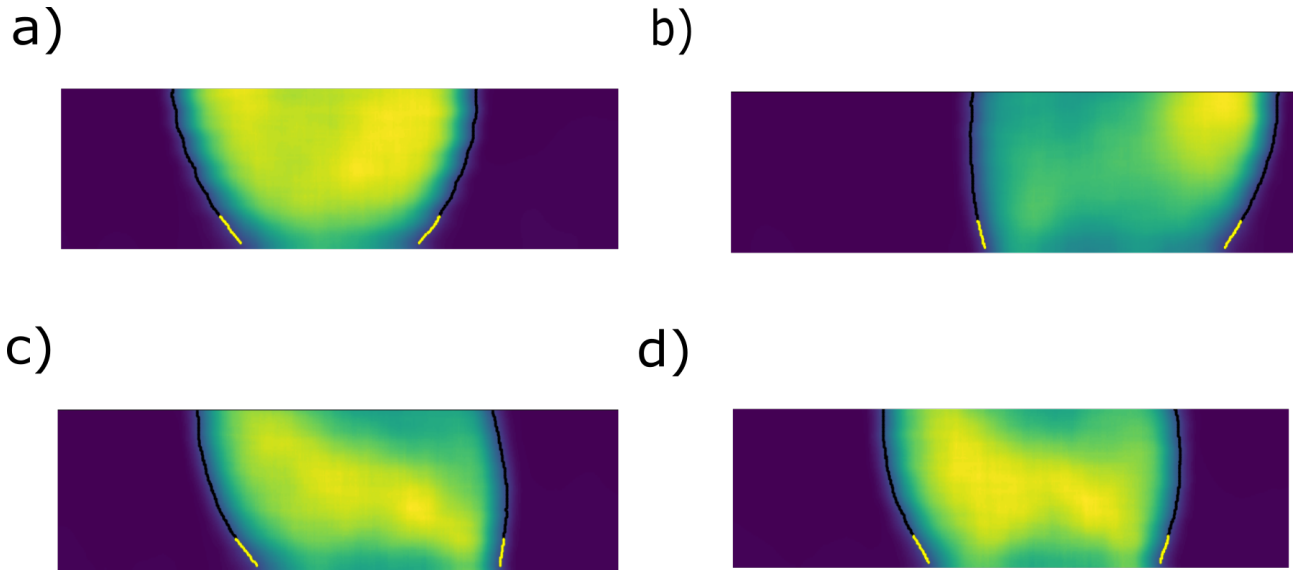

Figure 4.23: a) Drop before star the movement, we can appreciate the drop height, the static contact angle with the surface and the pinning radius. b) Drop going from the static to the dynamic regime. c) Drop retrace in the dynamic regime d) Drop coming back to the original position.

The LFM on the AFM give important information of the drop movement on the surface, we can have the friction force in time, see how the force map change in the different kinds of surfaces, and of course we can compare the force measurement values with the drop friction model showed in equation 1.9.

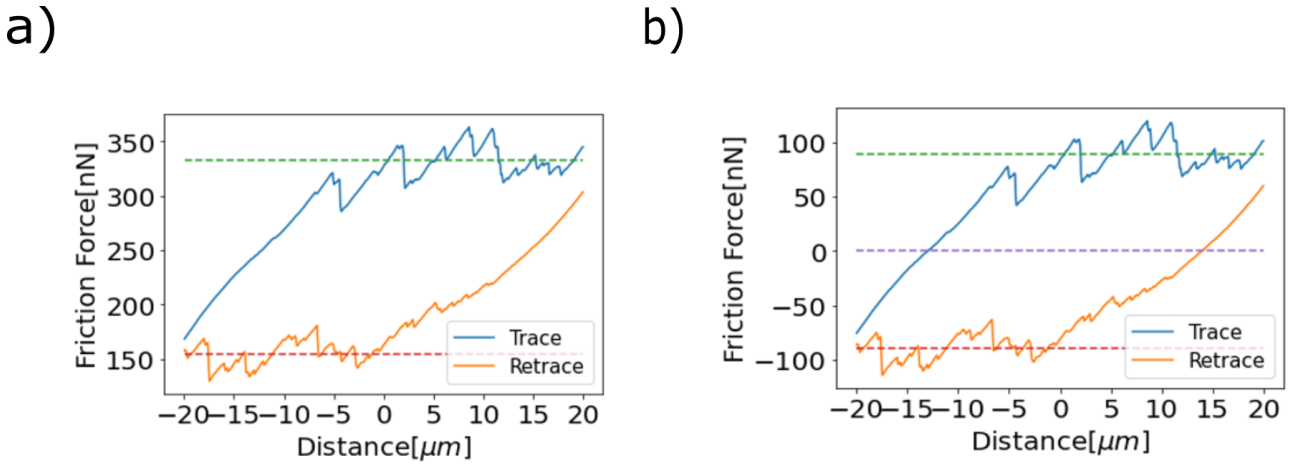

Figure 4.24: a) Original force curve, as we can see, the trace and retrace show positive values. b) Once the offset is corrected, we can appreciate that the values are more accurate in their physical behaviour

Using the same program implemented in the normal force measurement, we can extract the edge of the drop and make a fitting to obtain the CA hysteresis (Fig.4.25a) and the length of the drop in contact with the surface during the measurement (Fig.4.25b).

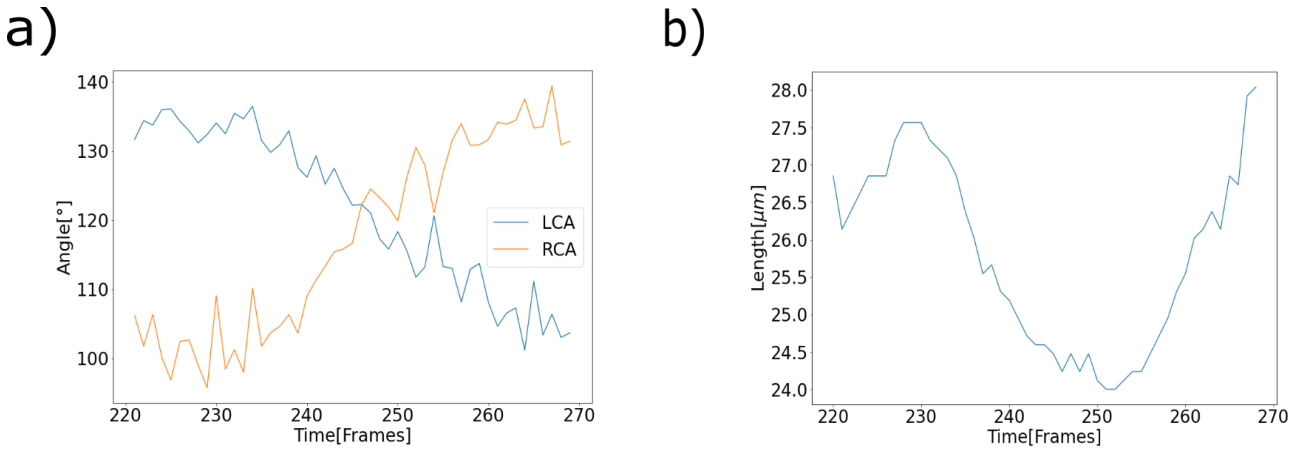

Figure 4.25: a) CA in Time: The left and right CA are showed in the graph, from this graph we can extract directly the contact angle hysteresis. b) Length in time: The length of the contact area with the drop is extracted directly from the fit. As we see, the length in time is not constant.

For the force, we use the friction model:

$$F_L = kL\gamma(\cos\Theta_{Re} - \cos\Theta_{Ad})$$

From the edge extraction we can obtain Θ and the length of the drop, in principle we use $k = 1$ and for L we took the half of the actual length, since experimental evidence has shown that this value tends to behave in this way [61]. Then we obtain the force in time showed in Fig.4.26.

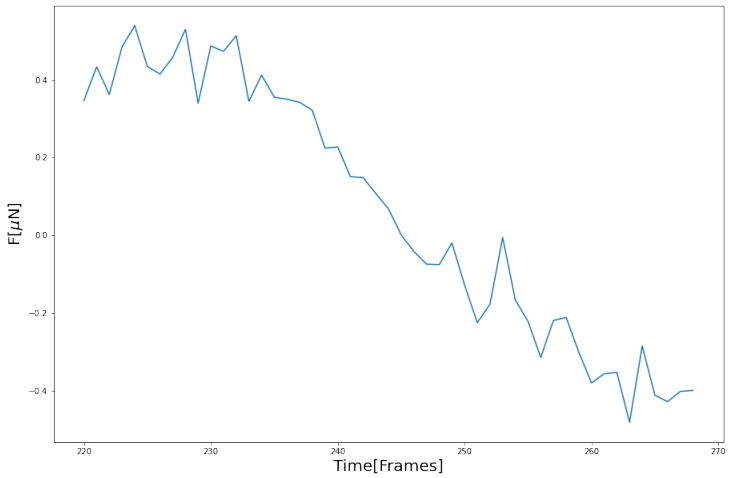

Figure 4.26: Force in time: The force in time follow the behaviour of the contact hysteresis, when there is no hysteresis, the friction force is zero.

Chapter 5

Conclusions and Future Work

Implementing simultaneous AFM and LSCM measurements give us several advantages when replicating macroscopic vertical and frictional force experiments at micro- and nanometric length scales. At these scales we were able to observe pinning and depinning processes that have not been been reported with macroscopic drops on superhydrophobic soot-template or nanofilament surfaces. We found that LSCM also turned out to be a useful tool for qualitative testing of superhydrophobic surfaces, allowing to observe remnant micro-droplets attached on the superhydrophobic and superamphiphobic surfaces. Lateral force AFM was used to measure friction, and we found that when we scale-down macroscopic drop experiments, pinning and depinning take a relevant role in the friction force, specially in the dynamic regime.

In terms of our surfaces, we used two types of liquids to test their quality. A first type of liquid we used were ionic liquids. A second liquid that was used was a water-glycerol mix, with which we achieved a stable dyed liquid that allowed reliable LCSM-AFM experiments. In general we found that good quality superhydrophobic surfaces leave no remnant drops after the liquid droplet is completely retracted. To make quantitative characterization of the surfaces, more research is necessary. A deeper analysis of the drop curvature using LSCM in time is of importance, given that it has a big influence on the capillary force. Nevertheless, obtaining the contact area and contact line with LSCM XY-imaging is a promising way to obtain information regarding the liquid interface. Using LSCM-AFM, we were able to measure the contact angle, the contact line, the pinning area and the drop shape. This allows us to calculate the forces and compare them with the actual values measured by the AFM. We were also able to qualitatively observe remnant drops on the surface, and the evaporation of these drops. We have shown the advantage of combining AFM with LSCM, obtaining important results to test the quality of superamphiphobic surfaces, and obtain quantitative results to describe the capillary adhesion phenomena. This helps us establish an important precedent for future measurements, where we look forward to characterise surfaces in a quantitative way, obtaining information about the surface energy and pinning phenomena.

Bibliography

[1] Kerstin Koch, Bharat Bhushan, and Wilhelm Barthlott. "Diversity of structure, morphology and wetting of plant surfaces". In: *Soft Matter* 4.10 (2008), pp. 1943–1963.

[2] Gregory S Watson, Marty Gellender, and Jolanta A Watson. "Self-propulsion of dew drops on lotus leaves: a potential mechanism for self cleaning". In: *Biofouling* 30.4 (2014), pp. 427–434.

[3] Qianqian Shang and Yonghong Zhou. "Fabrication of transparent superhydrophobic porous silica coating for self-cleaning and anti-fogging". In: *Ceramics International* 42.7 (2016), pp. 8706–8712.

[4] Bharat Bhushan, Yong Chae Jung, and Kerstin Koch. "Self-cleaning efficiency of artificial superhydrophobic surfaces". In: *Langmuir* 25.5 (2009), pp. 3240–3248.

[5] Jan Genzer and Kirill Efimenko. "Recent developments in superhydrophobic surfaces and their relevance to marine fouling: a review". In: *Biofouling* 22.5 (2006), pp. 339–360.

[6] Yuanyi Wang et al. "Verification of icephobic/anti-icing properties of a superhydrophobic surface". In: *ACS applied materials & interfaces* 5.8 (2013), pp. 3370–3381.

[7] LU Si et al. "Drag reduction in turbulent flows over superhydrophobic surfaces with micro-nano textures". In: *Mechanics in Engineering* 35.4 (2013), p. 20.

[8] Gh Barati Darband et al. "Science and engineering of superhydrophobic surfaces: review of corrosion resistance, chemical and mechanical stability". In: *Arabian Journal of Chemistry* 13.1 (2020), pp. 1763–1802.

[9] Shuhui Li et al. "A review on special wettability textiles: theoretical models, fabrication technologies and multifunctional applications". In: *Journal of Materials Chemistry A* 5.1 (2017), pp. 31–55.

[10] Takashi Kawano and Frank U Renner. "Studies on wetting behavior of hot-dip galvanizing process by use of model specimens with tailored surface oxides". In: *Surface and interface analysis* 44.8 (2012), pp. 1009–1012.

[11] CK Akkan et al. "Plasma and short pulse laser treatment of medical grade PEEK surfaces for controlled wetting". In: *Materials Letters* 109 (2013), pp. 261–264.

[12] Wen Li, Yanlong Zhan, and Sirong Yu. "Applications of superhydrophobic coatings in anti-icing: Theory, mechanisms, impact factors, challenges and perspectives". In: *Progress in Organic Coatings* 152 (2021), p. 106117.

[13] Edward Yu Bormashenko. "Wetting of real surfaces". In: *Wetting of Real Surfaces*. de Gruyter, 2018.

[14] William SY Wong et al. "Microdroplet contaminants: when and why superamphiphobic surfaces are not self-cleaning". In: *ACS nano* 14.4 (2020), pp. 3836–3846.

[15] Jeya Jeevahan et al. "Superhydrophobic surfaces: a review on fundamentals, applications, and challenges". In: *Journal of Coatings Technology and Research* 15.2 (2018), pp. 231–250.

[16] DW Pilat et al. “Dynamic measurement of the force required to move a liquid drop on a solid surface”. In: *Langmuir* 28.49 (2012), pp. 16812–16820.

[17] Benedict Samuel, Hong Zhao, and Kock-Yee Law. “Study of wetting and adhesion interactions between water and various polymer and superhydrophobic surfaces”. In: *The Journal of Physical Chemistry C* 115.30 (2011), pp. 14852–14861.

[18] Hans-Jürgen Butt, Brunero Cappella, and Michael Kappl. “Force measurements with the atomic force microscope: Technique, interpretation and applications”. In: *Surface science reports* 59.1-6 (2005), pp. 1–152.

[19] Dan Daniel et al. “Mapping micrometer-scale wetting properties of superhydrophobic surfaces”. In: *Proceedings of the National Academy of Sciences* 116.50 (2019), pp. 25008–25012.

[20] Hans-Jürgen Butt, Karlheinz Graf, and Michael Kappl. *Physics and chemistry of interfaces*. John Wiley & Sons, 2013.

[21] Rafael Tadmor. “Approaches in wetting phenomena”. In: *Soft Matter* 7.5 (2011), pp. 1577–1580.

[22] Thomas Young. “III. An essay on the cohesion of fluids”. In: *Philosophical transactions of the royal society of London* 95 (1805), pp. 65–87.

[23] HB Eral, DJCM t Mannetje, and Jung Min Oh. “Contact angle hysteresis: a review of fundamentals and applications”. In: *Colloid and polymer science* 291.2 (2013), pp. 247–260.

[24] Mathias Ahrenberg et al. “Vapor pressure of ionic liquids at low temperatures from AC-chip-calorimetry”. In: *Physical Chemistry Chemical Physics* 18.31 (2016), pp. 21381–21390.

[25] Abraham Marmur. “Superhydrophobic and superhygrophobic surfaces: from understanding non-wettability to design considerations”. In: *Soft Matter* 9.33 (2013), pp. 7900–7904.

[26] Diego Díaz et al. “How water wets and self-hydrophilizes nanopatterns of physisorbed hydrocarbons”. In: *Journal of colloid and interface science* 606 (2022), pp. 57–66.

[27] ABD Cassie. “Contact angles”. In: *Discussions of the Faraday society* 3 (1948), pp. 11–16.

[28] Wilhelm Barthlott and Christoph Neinhuis. “Purity of the sacred lotus, or escape from contamination in biological surfaces”. In: *Planta* 202.1 (1997), pp. 1–8.

[29] Robert N Wenzel. “Resistance of solid surfaces to wetting by water”. In: *Industrial & Engineering Chemistry* 28.8 (1936), pp. 988–994.

[30] Nan Gao et al. “How drops start sliding over solid surfaces”. In: *Nature Physics* 14.2 (2018), pp. 191–196.

[31] Charles W Extrand and Y Kumagai. “Liquid drops on an inclined plane: the relation between contact angles, drop shape, and retentive force”. In: *Journal of colloid and interface science* 170.2 (1995), pp. 515–521.

[32] Zonglin Chu and Stefan Seeger. “Superamphiphobic surfaces”. In: *Chemical Society Reviews* 43.8 (2014), pp. 2784–2798.

[33] Kock-Yee Law. *Definitions for hydrophilicity, hydrophobicity, and superhydrophobicity: getting the basics right*. 2014.

[34] Sumit Parvate, Prakhar Dixit, and Sujay Chattopadhyay. “Superhydrophobic surfaces: insights from theory and experiment”. In: *The Journal of Physical Chemistry B* 124.8 (2020), pp. 1323–1360.

[35] Avijit Das and Uttam Manna. “Customizing oil-wettability in air—without affecting extreme water repellency”. In: *Nanoscale* 12 (48 2020), pp. 24349–24356. doi: 10.1039/D0NR05964A. url: http://dx.doi.org/10.1039/D0NR05964A.

[36] Georg RJ Artus and Stefan Seeger. “One-dimensional silicone nanofilaments”. In: *Advances in colloid and interface science* 209 (2014), pp. 144–162.

[37] Junping Zhang and Stefan Seeger. “Superoleophobic coatings with ultralow sliding angles based on silicone nanofilaments”. In: *Angewandte Chemie International Edition* 50.29 (2011), pp. 6652–6656.

[38] Xu Deng et al. “Candle Soot as a Template for a Transparent Robust Superamphiphobic Coating”. In: *Science* 335.6064 (2012), pp. 67–70. doi: 10.1126/science.1207115. eprint: https://www.science.org/doi/pdf/10.1126/science.1207115. url: https://www.science.org/doi/abs/10.1126/science.1207115.

[39] Evgeny V Shun’ko and VS Belkin. “Cleaning properties of atomic oxygen excited to metastable state 2 s 2 2 p 4 (S 1 0)”. In: *Journal of Applied Physics* 102.8 (2007), p. 083304.

[40] Walid-Madhat Munief et al. “Silane deposition via gas-phase evaporation and high-resolution surface characterization of the ultrathin siloxane coatings”. In: *Langmuir* 34.35 (2018), pp. 10217–10229.

[41] JB Brzoska, I Ben Azouz, and F Rondelez. “Silanization of solid substrates: a step toward reproducibility”. In: *Langmuir* 10.11 (1994), pp. 4367–4373.

[42] Debbie Stokes. *Principles and practice of variable pressure/environmental scanning electron microscopy (VP-ESEM)*. John Wiley & Sons, 2008.

[43] Nestor J Zaluzec. “Quantitative X-ray microanalysis: Instrumental considerations and applications to materials science”. In: *Introduction to analytical electron microscopy*. Springer, 1979, pp. 121–167.

[44] S Zaefferer. “A critical review of orientation microscopy in SEM and TEM”. In: *Crystal Research and Technology* 46.6 (2011), pp. 607–628.

[45] John Melngailis. “Focused ion beam technology and applications”. In: *Journal of Vacuum Science & Technology B: Microelectronics Processing and Phenomena* 5.2 (1987), pp. 469–495.

[46] P Lecomte Du Noüy. “An interfacial tensiometer for universal use”. In: *The Journal of general physiology* 7.5 (1925), p. 625.

[47] K Lunkenheimer and K-D Wantke. “Determination of the surface tension of surfactant solutions applying the method of Lecomte du Noüy (ring tensiometer)”. In: *Colloid and Polymer Science* 259.3 (1981), pp. 354–366.

[48] Ch Gerber, CF Quate, and G Binning. “Atomic force microscope”. In: *Phys. Rev. Lett* 56 (1986), pp. 930–933.

[49] Werner A Hofer, Adam S Foster, and Alexander L Shluger. “Theories of scanning probe microscopes at the atomic scale”. In: *Reviews of Modern Physics* 75.4 (2003), p. 1287.

[50] William A Ducker, Tim J Senden, and Richard M Pashley. “Direct measurement of colloidal forces using an atomic force microscope”. In: *Nature* 353.6341 (1991), pp. 239–241.

[51] Michael Kappl and Hans-Jürgen Butt. “The colloidal probe technique and its application to adhesion force measurements”. In: *Particle & Particle Systems Characterization: Measurement and Description of Particle Properties and Behavior in Powders and Other Disperse Systems* 19.3 (2002), pp. 129–143.

[52] Raymond R Dagastine et al. “Forces between two oil drops in aqueous solution measured by AFM”. In: *Journal of colloid and interface science* 273.1 (2004), pp. 339–342.

[53] Martin Benoit et al. “Discrete interactions in cell adhesion measured by single-molecule force spectroscopy”. In: *Nature cell biology* 2.6 (2000), pp. 313–317.

[54] Chen Shi et al. “Interaction mechanism of oil-in-water emulsions with asphaltenes determined using droplet probe AFM”. In: *Langmuir* 32.10 (2016), pp. 2302–2310.

[55] Chen Shi et al. “Probing the hydrophobic interaction between air bubbles and partially hydrophobic surfaces using atomic force microscopy”. In: *The Journal of Physical Chemistry C* 118.43 (2014), pp. 25000–25008.

[56] Christopher P Green et al. “Normal and torsional spring constants of atomic force microscope cantilevers”. In: *Review of Scientific Instruments* 75.6 (2004), pp. 1988–1996.

[57] John Elie Sader. “Frequency response of cantilever beams immersed in viscous fluids with applications to the atomic force microscope”. In: *Journal of applied physics* 84.1 (1998), pp. 64–76.

[58] John E Sader, James WM Chon, and Paul Mulvaney. “Calibration of rectangular atomic force microscope cantilevers”. In: *Review of scientific instruments* 70.10 (1999), pp. 3967–3969.

[59] Christopher P Green and John E Sader. “Torsional frequency response of cantilever beams immersed in viscous fluids with applications to the atomic force microscope”. In: *Journal of applied physics* 92.10 (2002), pp. 6262–6274.

[60] Marvin Minsky. “Memoir on inventing the confocal scanning microscope”. In: *Scanning* 10.4 (1988), pp. 128–138.

[61] MJ Santos, S Velasco, and JA White. “Simulation analysis of contact angles and retention forces of liquid drops on inclined surfaces”. In: *Langmuir* 28.32 (2012), pp. 11819–11826.